**Research Article**

## applied optics

# Design of a monolithic Michelson interferometer for fringe imaging in a near-field, UV, direct-detection Doppler wind lidar

**Jonas Herbst\* and Patrick Vrancken**

*Institut für Physik der Atmosphäre (IPA), German Aerospace Center (DLR), Oberpfaffenhofen, Münchener Str. 20, 82234 Weßling, Germany*
*Corresponding author: jonas.herbst@dlr.de*

The low-biased, fast, airborne, short-range, and range-resolved determination of atmospheric wind speeds plays a key role in wake vortex and turbulence mitigation strategies and would improve flight safety, comfort, and economy. In this work, a concept for an airborne, UV, direct-detection Doppler wind lidar receiver is presented. A monolithic, tilted, field-widened, fringe-imaging Michelson interferometer (FWFIMI) combines the advantages of low angular sensitivity, high thermo-mechanical stability, independence of the specific atmospheric conditions, and potential for fast data evaluation. Design and integration of the FWFIMI into a lidar receiver concept are described. Simulations help to evaluate the receiver design and prospect sufficient performance under different atmospheric conditions. © 2016 Optical Society of America

*OCIS codes:* (280.3640) Lidar; (120.3180) Interferometry; (280.3340) Laser Doppler velocimetry; (280.7060) Turbulence.

http://dx.doi.org/10.1364/AO.55.006910

## 1. INTRODUCTION

Wake vortices, gusts, and turbulence in clear air impose a major risk in commercial air transport because onboard weather radars cannot detect turbulence in clear air [1]. Recent radars provide some turbulence detection functionality in the presence of clouds and precipitation [2]. If encountered by another aircraft, turbulence can cause unexpected rolling moments or abrupt changes of altitude, which may result in damage to the plane or injuries to the passengers [3,4].

In particular, wake vortices are a well-studied phenomenon since their discovery in the early 20th century. Two rotating, long-life vortices are produced at the wing tips of any aircraft. Today's traditional risk reducer is a standard minimum distance of travel between any two planes, which is chosen according to the aircrafts' weights, such that the vortices have safely decayed or subsided before the encounter. One way to meet the ongoing trend of increasing passenger numbers is to increase the timing frequency between any two planes without a reduction of safety. Plate lines are a concept to increase the decay rate of wake vortices that works only in ground proximity [5]. Further possibilities to reach this goal include a direct reaction to the forces of the wake vortex on the aircraft by new flight controller routines, examined by Looye *et al.* [6], or the remote sensing of the disturbances caused by wake vortices and turbulences.

Remote sensing is the only means for measuring wind vectors in the near field (50–300 m), ahead of the aircraft.

This would allow for a fast reaction of the flight controller (autopilot) [7,8]. Ehlers *et al.* deem a full-scan update rate of the wind field measurement of 5–10 Hz appropriate for their concept of wake impact alleviation control to work reasonably well at a range of 60 m [8,9]. The control concept includes a wake identification algorithm, which allows one to reconstruct the wake vortex disturbance, and alleviates its impact by specific control commands to compensate for the determined disturbance. After a computation time of 200 ms for the first identification of the wake vortex, the control system continuously (typical sampling time in the order of 20 ms [9]) countervails the disturbances on the basis of the determined wake vortex model. Note that the disturbance reconstruction step allows the anticipation of the disturbances at locations where no measurement was made (or not yet), leading to rather complex relationships between the sensor measurements (location, orientation, and quality) and the disturbance rejection capability [8]. Actuator time delays, which are assumed to be 100 ms, are compensated by predicting the wake vortex impact on the aircraft for a moment 100 ms in the future [9]. This control concept can be applied in very similar ways for the mitigation of wake vortices, gusts, and turbulences [10].

However, currently, no reliable sensing system for onboard measurements of wind speeds exists, which could guarantee that the safety standards of the International Civil Aviation Organization are met in such a future scenario.

Amongst the remote sensing devices, lidar has the advantage of speed and high local precision. Doppler wind lidars (DWL) measure frequency changes caused by the Doppler effect of molecules and aerosols moving with the ambient wind in order to derive wind speed components along the line-of-sight (LoS) of the laser beam. A distinction can be made between coherent and incoherent (direct) DWLs.

Coherent DWLs often use IR laser light, which provides sensitivity to backscatter from micron-sized aerosols [11,12]. Furthermore, IR laser technology is reliable and often asserted eye-safe depending on the laser parameters, e.g., at low pulse energies and low exposure durations [13]. The Doppler-shifted signal scattered mainly from aerosols is superimposed coherently with a frequency-shifted reference (local oscillator). The Doppler shift is determined from the beat frequency by a fast Fourier transform from the power density spectrum. Systems with $CO_2$-lasers, Tm:LuAG-lasers, and with Er-doped fiber lasers have successfully been applied to measure wind speeds at the ground level and in the boundary layer [14–16]. Turbulence detection in the troposphere at an altitude of 12 km with a coherent DWL has been demonstrated up to 9 km ahead of an aircraft with a range bin of 150 m [17]. At these high altitudes, the concentration of aerosols is low and the coherence of the received signal is reduced, which decreases the signal-to-noise ratio (SNR) and the maximum range of detection. As a consequence of the Fourier limit and the required coherence (small spectral bandwidth) properties of the laser, the minimal pulse length and the spatial resolution are limited [11], e.g., 170 ns and 30 m and a minimum detection range of 150 m for the Halo Photonics 1.5-μm Streamline pulsed coherent Doppler lidar [18].

Coherent DWLs have not yet been demonstrated to measure wind speeds reliably at high cruise flight altitudes (12 km) or in clear air and with short range bins (15–30 m) in the near field (50–300 m in front of an aircraft). Accurate range-resolved LoS wind speed measurements with standard deviations of approx. 1 ms$^{-1}$ with comparable lidar geometry parameters would be required for reliable feed-forward control, as pointed out in a lidar parameter study by Ehlers et al. [8].

Although coherent DWLs might still be an option, only direct-detection DWLs are considered from now on, because they can rely on pure molecular scattering, pure scattering from aerosols or a combination, and because the range gate length can be made smaller than 30 m. Direct-detection DWLs may consist of filters, which transmit only a certain spectral bandwidth. From the amount of light that is transmitted through the filters, the Doppler frequency shift can be determined.

Iodine-vapor DWLs using absorption bands of iodine as filters are limited to a laser wavelength of 532 nm. In airborn lidar, UV wavelengths ($\lambda$) are preferred, because UV systems may be designed eye-safe beyond a certain, acceptable distance (see, e.g., [19]) and because of the high efficiency of Rayleigh scattering in the UV, which is roughly proportional to $\lambda^{-4}$ (see Section 2.A).

The double-edge technique (DE) is based on two Fabry–Perot interferometers with different optical path lengths that determine the frequency of maximum transmission. The Doppler shift is determined by the ratio of transmission

through these filters [20]. The transmission through the filters strongly depends on the shape of the light scattering spectra, which is why this method requires the knowledge of the altitude (backscatter ratio, temperature, pressure). In practice, the required separation of the Rayleigh and Mie channels, e.g., used in ALADIN [21], can only be circumvented by the use of multiple filters or the equivalent fringe-imaging technique (FI). These FI techniques have the main advantage that measurements can be performed without knowledge of the shape of the backscattered signal spectrum.

The principle of fringe imaging relies on the imaging of the interference pattern of an interferometer on a position-sensitive detector. The frequency shift between an unshifted reference and a Doppler-shifted signal can be determined from the dislocation of the interference pattern. A distinction can be made between multi-wave and two-wave interference. The most common multi-wave interferometer is the Fabry–Perot interferometer (FPI). When properly illuminated with divergent light, the produced interference fringes are rings. As the light is Doppler shifted, the radii of the rings change. This principle was applied in the AWIATOR ("Aircraft Wing with Advanced Technology Operation") project [22,23]. However, the evaluation of the interference patterns is delicate, time consuming, and prone to errors due to possible dislocations of the ring centers on a two-dimensional CCD array [24]. Furthermore, typical two-dimensional detectors, such as CCD, are too slow for range-resolved detection.

Other interferometers are designed with an inclination of one of their mirrors to produce a pattern of linear interference fringes. The shift of the linear fringe can be determined with fast, linear detectors.

A multi-wave type is the Fizeau interferometer. The complex fringe shape of a deformed Airy can be accounted for by the use of proper system parameters [25]. The fringe shape depends strongly on the field angle of the incident light, but the deformation and contrast loss impede us from being able to use it with extended sources, as in the presently described application (see Section 3.A).

For the purpose of collecting range-resolved backscattered light in close range (50–300 m) in front of the aircraft with an equivalent region of total overlap, a telescope with a large field of view (FOV) (about 4 mrad) is required. This large FOV produces, independent of the setup design (free beam or fiber coupled), an important angular distribution after collimation. The interferometer needs to be field widened in order to accept a broad range of incident angles without a loss of contrast.

The necessary field widening can be realized with two-wave interferometers. Liu and Kobayashi proposed to use a Mach–Zehnder interferometer in a direct-detection DWL, using a two-channel differential discrimination method (DMZ), similar to the DE technique using the FPI [26]. Bruneau considered a four-channel-based version (QMZ) [27] and an equivalent field-widened fringe-imaging Mach–Zehnder interferometer with inclined mirrors (FIMZ) [28], both optimized for Rayleigh scattering. Bruneau and Pelon showed that the concept can be used to measure wind speeds [29]. An application of this principle is Ball Aerospace and Technologies Corp.'s

Optical Autocovariance Wind Lidar [30], which was proposed to measure wind speeds from the international space station [31]. Recently, a modified DMZ using three wavelengths was proposed for an Fe Doppler lidar for wind measurements from ground to thermosphere [32].

Multiple filters can be created with a Michelson interferometer as well. Cezard *et al.* considered a dual fringe-imaging Michelson interferometer (FIMI) with inclined mirrors for the measurement of the wind speed and other air parameters (temperature, scattering ratio, density) [33].

The monolithic Michelson interferometer design we present in this work is based on the same fringe-imaging principle. In contrast to the cited test setup, our field-widened, fringe-imaging Michelson interferometer (FWFIMI) design provides, however, the thermo-mechanical stability and design features necessary for fast, range-resolved, and airborne measurements of wind speeds in the near field in front of an aircraft. The advantages of a monolithic FIMI are detailed more closely below.

There is a long tradition of the design and application of monolithic, "field-widened Michelson interferometers" (FWMI) or "wide-angle Michelson interferometers" (WAMI). The basic idea of FWMI was developed in 1941 [34]. FWMIs can be built temperature compensated as solid model, where the two interferometer arms consist of different glasses at a certain length ratio, or as air-spaced models, where the air arm mirror is fixed by spacers of the same or different materials as the glass arm and may be positioned with a piezo feedback control. They have been realized with cube [35] or hexagonal beam splitters [36] and as a Doppler asymmetric spatial heterodyne version [37], just to name a few.

For the presently considered application of measuring LoS wind speeds that are range resolved in the near field, we consider only two-wave interferometers to be adequate. In particular we consider a FIMI for the following reasons: first, a FIMI with slanted mirrors produces linear fringes, which can be imaged on fast, linear detectors for range-resolved detection. Secondly, airborne interferometers call for stability with respect to vibrations and temperature. An FIMI is more easily built in a monolithic way than an FIMZ. Third, a monolithic FIMI can be constructed to be both field widened (FWFIMI) and temperature compensated. Finally, our design of a monolithic FWFIMI can be arranged to be tilted to the incident light, enabling a two-channel operation, in which case the FIMI can reach the theoretical performance of the FIMZ (see Section 2.B).

The proposed measurement concept is detailed more closely in the following, considering certain assumptions: we consider different lidar transmitters (lasers) used in WALES/DELICAT ("WAter vapor Lidar Experiment in Space" project/ "Demonstration of LIdar based Clear Air Turbulence" project) [38,39], AWIATOR [23], and MULTIPLY (ESA project). We assume a moderately sized, airborne-compatible telescope of about 15 cm diameter in a monostatic configuration. Two receiver concepts are presented: free beam and fiber coupled. In a free-beam arrangement, the image of the fringes on the detector is range dependent and changes with the misalignment of the laser beam with respect to the telescope (see Section 3.A).

Even with a field-widened interferometer, a fiber-coupled design may be preferred in the context of bias reduction [40] in comparison to a free-beam setup (see Section 3.A). In a fiber-coupled setup, the backscattered collimated light is coupled into a large-core multimode fiber. The scrambling properties of the fiber produce a constant far field of the out-coupled light and a constant illumination of the interferometer, independent of the position and the angular orientation of the light focused on the multimode fiber core during coupling (see Section 4). The fiber-coupled concept is enhanced by the application of a two-lens optical scrambler to increase the far-field scrambling gain [41] and by mechanical vibrations for speckle reduction. Because of the finite extension of the fiber core, the recollimated light is expected to come by a centered range- and misalignment-independent angular distribution. The FWFIMI has a net inclination angle fixed such that one linear fringe is imaged on a linear detector, which allows range-resolved measurements in the near field in front of the aircraft.

To begin with, we summarize in Section 2 the fundamentals of light scattering and of the FIMI as a direct-detection DWL, and we compare the theoretical performances of different direct-detection DWLs for the measurement of wind speeds. In Section 3, the lidar geometry requirements and all aspects of our design of a temperature-compensated FWFIMI are described in detail. In Section 4, the integration of the FWFIMI in a lidar receiver prototype for the measurement of wind speeds in the near field is detailed. In Section 5, we evaluate the proposed receiver concept in terms of expected performance, using simulations, while taking into account the detector and speckle noise during the data evaluation.

## 2. FUNDAMENTALS

### A. Atmospheric Backscattering Spectrum and Single-Scattering Lidar Equation

The atmospheric backscattering spectrum has contributions from light scattering by molecules ("Rayleigh–Brillouin" scattering, rotational and vibrational Raman scattering) [42] and from light scattering by aerosols/hydrometeors. The Rayleigh–Mie-Laser spectrum (RMLS) is introduced here to model the spectral contributions from Rayleigh–Brillouin scattering by molecules, from scattering by spherical particles [43] and from the lineshape of the laser as Gaussian-shaped lines [24].

The quasi-elastic molecular ("Rayleigh–Brillouin") scattering spectrum (the so-called Cabannes line composed of the Landau–Placzek line and the Brillouin doublet) is the result of coherent scattering, which dominates molecular scattering, and therefore, the scattered light is mostly polarized [44]. For a DWL only, this central part is considered. The shape of the Cabannes line depends on the density of the scatterers. Accordingly, different regimes (hydrodynamic: e.g., gas-liquid mixtures [45], kinetic: atmosphere, and Knudsen: thin gases) can be discriminated. If the mean free path between the thermally moving molecules is large, a Gaussian lineshape (Knudsen) can be assumed. As the pressure increases and the temperature decreases, density fluctuations moving at acoustic speeds deform the lineshape (kinetic regime), until at the

hydrodynamic limit, two acoustic side bands (Brillouin lines) appear.

The scattering properties of aerosols in the atmosphere, such as the lidar ratio and particle depolarization rato, are highly dependent on their type and shape, and there is large variability [46]. Here, the simplifying assumption of spherical particles is made (the Mie theory is valid only for spherical particles [43]). This allows us to describe the backscattering from aerosols as purely elastic and without depolarization.

In our simulations in Section 5, we consider an approximation of the (kinetic) S6 model [47]. It describes the kinetic regime by the sum of three Gaussian functions (henceforth called the G3 model) [48]. Here, for a simple analytical description of the theoretical performance of the FIMI, the Knudsen model (neglecting the Brillouin doublet) is presented in the following to produce the RMLS. The neglected Brillouin contribution does not affect the spectrum's central frequency and has therefore no effect on the performance of the wind speed measurements [33]. Furthermore, there is no effect on the contrast factor G in the vicinity of the optimal FSR determined in Section 5.B.

The RMLS consists of the weighted sum of the Gaussian molecular scattering peak and the Gaussian aerosol scattering peak, convolved with the Gaussian laser lineshape,

$$I_{\mathrm{RMLS}}(\nu) = \frac{1}{R_b} \frac{1}{\sqrt{2\pi}\sigma_G} \exp\left[-\left(\frac{\nu - \nu_c}{\sqrt{2}\sigma_G}\right)^2\right]$$
$$+ \left(1 - \frac{1}{R_b}\right) \frac{1}{\sqrt{2\pi(\sigma_L^2 + \sigma_w^2)}} \exp\left[-\left(\frac{\nu - \nu_c}{\sqrt{2}\sqrt{\sigma_L^2 + \sigma_w^2}}\right)^2\right].$$
(1)

Here, $R_b$ is the particle scattering ratio given by $R_b = 1 + \beta_{\mathrm{Mie}}/\beta_{\mathrm{Ray}}$ with the Mie and Rayleigh backscattering coefficients [m$^{-1}$ sr$^{-1}$] $\beta_{\mathrm{Mie}}$ and $\beta_{\mathrm{Ray}}$. Values of $\beta_{\mathrm{Ray}}$ for different altitudes ($H$) can be obtained by $\beta_{\mathrm{Ray}} = p(H)/(R_{\mathrm{air}} T(H) m_{\mathrm{air}}) \times (550/\lambda_L[\mathrm{nm}])^4 \times 5.45 \times 10^{-32}$ after Collis and Russell [49], where $p(H)$ and $T(H)$ are altitude-dependent pressures and absolute temperatures obtained from an atmospheric model. Here, $R_{\mathrm{air}} = 287.058$ J/kgK is the gas constant of air, and $m_{\mathrm{air}} = 4.811 \times 10^{-26}$ kg is the mass of an air molecule. A more complete model provided by Bucholtz [50] includes the dispersion of the refractive index of air, the anisotropy of air molecules, and the dispersion of the depolarization factor of air. The differential scattering cross section and backscattering coefficients calculated with the simplified model stated above are 4.5% smaller than those calculated by Bucholtz. This approximation has, however, a negligible influence on the absolute values of the signal-to-noise ratios calculated in Section 5 (deviation: $\approx 2.3\%$). The values of $\beta_{\mathrm{Mie}}$ are scaled from values determined by Vaughan at 10.6 µm [51], using $\beta_{\mathrm{Mie}}$ are scaled from values determined by Vaughan at 10.6 µm [51], using $\beta_{\mathrm{Mie}} = \beta_{\mathrm{Mie}}[10.6\,\mu\mathrm{m}] \times (10.6/\lambda_L[\mu\mathrm{m}]) \times (-0.104 \times \ln(\beta_{\mathrm{Mie}}[10.6\,\mu\mathrm{m}])) - 0.62$. The total backscattering coefficient is $\beta = \beta_{\mathrm{Ray}} + \beta_{\mathrm{Mie}}$. The Doppler shift [Hz] is defined as $\Delta\nu = \nu_c - \nu_L = 2\nu_L u_r/c$, where $\nu_L$ is the frequency of the laser, $\nu_c$ is the Doppler-shifted central frequency, and $u_r$ is the LoS wind speed. $\sigma_L = \Delta\nu_L/\sqrt{8 \ln 2}$ is the standard deviation [Hz] of the Gaussian laser line

shape, where $\Delta\nu_L$ is the laser linewidth (FWHM) [Hz]. $\sigma_G = (\sigma_{\mathrm{Ray}}^2 + \sigma_L^2)^{1/2}$ is the standard deviation in Hz of the Rayleigh–Laser spectrum, whereby $\sigma_{\mathrm{Ray}} = 2/\lambda_L((k_B T N_A)/m_{\mathrm{air}})^{1/2}$ is the standard deviation in Hz of the Rayleigh spectrum, where $k_B$ is the Boltzmann constant, $N_A$ is the Avogadro constant, and $T$ is the air temperature in the scattering volume. $\lambda_L$ is the wavelength of the laser. $\sigma_w = \sqrt{4/3}/\nu_L u_{\mathrm{r.m.s}}$ is the broadening due to the r.m.s. wind speed $u_{\mathrm{r.m.s}}$ at flight level. Typical, conservative values of $u_{\mathrm{r.m.s}}$ and $\sigma_w$ at $H = 30$–$40,000$ ft are 1.7 m/s [52] and 5.5 MHz for moderate turbulence, which is about 3% as broad as the WALES transmitter lineshape.

The amount of backscattered light received by the lidar is calculated with the single-scattering lidar equation [53] in a monochromatic approximation. The amount of time-resolved EM wave power detected, imagined here as number of photons per range gate $n_p$ (no assumptions on the nature of light) [54] is given by

$$n_p(\nu_L, R) = E_L \frac{\Delta R}{h\nu_L} \frac{A}{R^2} \xi(r)\eta_R \eta_T \beta \exp\left(-2\int_0^R \alpha \mathrm{d}r\right). \quad (2)$$

Here, $R$ is the distance [m] of the light scattering volume in front of the telescope. $\Delta R$ is the length [m] of the range gate. $E_L$ is the transmitted energy of one laser pulse with pulse duration $\tau_p$. $h = 6.626(10)^{-34}$ Js is Planck's constant. $A$ is the receiver telescope area [m$^2$]. $\xi(r)$ is the range-dependent overlap function. $\eta_R$ and $\eta_T$ are the receiver and transmitter loss factors. $\alpha = \alpha_{\mathrm{Ray}_s} + \alpha_{\mathrm{Ray}_a} + \alpha_{\mathrm{Mie}}$ is the overall atmospheric extinction coefficient [1/m], where $\alpha_{\mathrm{Ray}_s} = 8\pi/3\beta_{\mathrm{Ray}}$ is the molecular extinction [1/m], $\alpha_{\mathrm{Ray}_a}$ is the molecular absorption [1/m], and $\alpha_{\mathrm{Mie}}$ is the extinction and absorption by aerosols. For monodispersed spherical particles, the aerosol extinction is $\alpha_{\mathrm{Mie}} = k'\beta_{\mathrm{Mie}}$ [55]. Here, a constant extinction-to-backscatter ratio of $k' = 50$ sr is assumed.

## B. Theoretical Performance of a Fringe-Imaging Michelson Interferometer

In this section, the principle of direct-detection DWLs based on the FIMI is summarized, and the FIMI's optimized theoretical performance is compared with other direct-detection DWL methods.

The monochromatic transmission function (TF) of a Michelson interferometer with inclined mirrors is cosine shaped and varies in space along the $x$-axis. It can be written as

$$I(x, y, \nu) = \mathrm{FI}_0[1 + V \cos(\phi)]. \quad (3)$$

Here, the linear interference fringes are aligned perpendicular to the $x$-axis and parallel to the $y$-axis. $V$ is the instrumental interference contrast; its contributions are described in Section 3.E and F. $\phi = (2\pi\nu)/c(\mathrm{OPD}_0 - 2\theta x)$ is the fringe phase. $\mathrm{OPD}_0$ is the fixed optical path length difference between the arms. Assuming dispersion-free media in the interferometer arms, $\mathrm{OPD}_0$ is equal to $c/\mathrm{FSR}$, where FSR is the free spectral range. The FSR is the width of one fringe period in [Hz]. $\theta$ is the angle of inclination in the $x$-direction rotated along the $y$-direction. $\theta$ creates a linear variation of $\mathrm{OPD}_0$ within the illuminated area of width $d_w$. It determines the amount of periods $N_p$ of the TF. To image exactly $N_p$ fringe periods, $\theta$ equals $N_p\lambda_L/(2d_w)$. The prefactor $F = 0.5$ accounts for the reflection losses of a

Michelson interferometer. The instrument function is the convolution of the laser lineshape with the TF. The received instrument function ($I_F$) is the convolution of the RMLS [Eq. (1)] with the TF [Eq. (3)]:

$$I_F(x, y, \nu) = \text{FI}_0[1 + W(T, \alpha) \cos(\phi + \Delta\phi)]. \qquad (4)$$

The resulting interference pattern is shifted in phase by $\Delta\phi = 4\pi/(\text{FSR}\lambda_L)u_r$ and has a reduced global fringe contrast $W(T, \alpha) = V \times G(\text{FSR})$, where

$$G(\text{FSR}) = \exp\left[-2\left(\frac{\pi\Delta\nu_L}{\text{FSR}}\right)^2\right]$$

$$\times \left(\frac{1}{R_b}\exp[-2(\pi\sigma_{\text{Ray}}/\text{FSR})^2] + \left(1 - \frac{1}{R_b}\right)\right). \qquad (5)$$

The LoS wind speed $u_r$ is determined by measuring the phase shift $\Delta\phi$ between a reference instrument function and a Doppler frequency-shifted received instrument function, which are both imaged sequentially on a position-sensitive detector.

In the above description, the FIMI is a multichannel spectral analyzer. A general way to find the optimal FSR setting of the FIMI for the measurement of wind speeds is to introduce a penalty factor $\kappa_{\text{VLOS}}$, comparing the interferometer with an ideal spectral analyzer (ISA). An ISA performs the perfect spectral analysis because it is composed of an infinite number of sampling channels, which sample the spectrum with Dirac-type transmission functions. In an ISA, there is no loss of information, energy, or spectral content. An interferometer (like the FIMI) mixes the photons spatially and spectrally and therefore underperforms compared to the ISA.

Bruneau and Cezard *et al.* derived expressions for the optimal fixed optical path difference of the fringe-imaging Mach–Zehnder interferometer ($\text{OPD}_{\text{FIMZ}} \approx 3$ cm at 250 K) [28] and the fringe-imaging Michelson interferometer ($\text{OPD}_{\text{FIMI}} = 2.8$ cm at $R_b = 1$, $T = 273$ K) [33], respectively.

The penalty factor $\kappa_{\text{VLOS}}$ (by Cezard *et al.* for pure Rayleigh scattering) compares the Cramer–Rao bounds (CRBs) of the FIMI and the ISA. The CRBs are the respective lowest-achievable standard deviations of an unbiased estimator. Cezard *et al.* used a maximum-likelihood estimator approach (which asymptotically reaches the CRB) for inversion and obtained the CRBs of the wind speed as diagonal elements of the inverse Fischer matrices of the FIMI and the ISA. The underlying assumptions are that the signal is shot-noise limited, obeys a Poisson statistic, and that the different channels are statistically independent. $\kappa_{\text{VLOS}}$ can be written as a function of the FSR,

$$\kappa_{\text{VLOS}} = \frac{\varepsilon_{\text{FIMI}}}{\varepsilon_{\text{ISA}}}$$

$$= \frac{d_c\text{FSR}}{\sqrt{2}c}\left(1 - \sqrt{1 - V^2 \exp\left[-8\frac{c}{d_c\text{FSR}}\right]^2}\right)^{-1/2}. \qquad (6)$$

Here, $\varepsilon_{\text{FIMI}}$ and $\varepsilon_{\text{ISA}}$ are the CRBs for the FIMI and the ISA. $d_c = 2c/(\pi\sigma_{\text{Ray}}\sqrt{T})$ is the coherence length of the Rayleigh signal. If the FSR is too large, the fringe phase sensitivity $S = 4\pi/(\text{FSR}\lambda_L)$ in rad/(m/s) with respect to the Doppler shift is small. If the FSR is too small, the fringe contrast is too small for an efficient determination of the fringe phase. The FSR is optimized for the "worst" condition, where no aero-
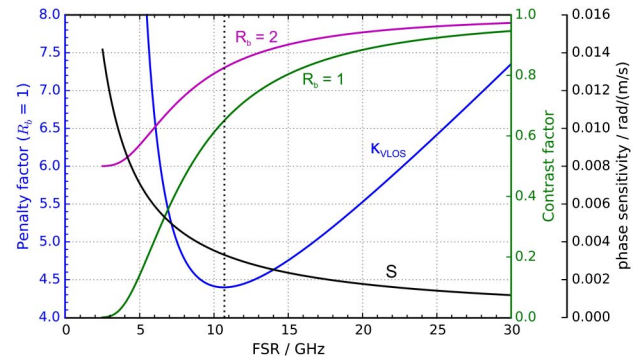


**Fig. 1.** Penalty factor of wind speed measurement $\kappa_{\text{VLOS}}$ (blue), contrast factor G(FSR) (green: $R_b = 1$, magenta: $R_b = 2$), and phase sensitivity S (black) as a function of FSR for 273 K, $R_b = 1$ at a wavelength of 355 nm.

sols contribute to backscattering ($R_b = 1$). Here, the contrast factor $G$ is equal to 66%. In Fig. 1, $\kappa_{\text{VLOS}}$ is plotted as a function of the FSR at 273 K for $R_b = 1$. The plot includes contrast factors $G(\text{FSR})$ for $R_b = 1$ (green) and $R_b = 2$ (magenta) and the phase sensitivity $S(\text{FSR})$ (black).

Cezard *et al.* showed that when $R_b$ increases, the global contrast increases, thus producing lower penalty factors, and that a decrease of the temperature by 40 K decreases $\kappa_{\text{VLOS}}$ by 10% [33]. The best measurement performance is thus expected at low temperatures and high scattering ratios. The optimal FSR value of 10.7 GHz $\approx 6.8 \times \sigma_{\text{Ray}}$ (at $R_b = 1$, $T = 273$ K) is found at the minimum: $\kappa_{\text{VLOS}} = 4.4$ (dotted line).

Table 1 lists the penalty factors of other DWL techniques obtained in similar ways for comparison.

The two filter-based techniques, the double-edge Fabry–Perot (DFP) and the DMZ, have good theoretical performance, but they are sensitive to the Rayleigh–Mie backscattering scattering ratio and require inversion of the lidar signal to correct this [27]. The fringe-imaging Fabry–Perot technique (FIFP) is complicated by the evaluation of circular fringe patterns or the complexities of circle-to-line converters [59]. The fringe-imaging Fizeau interferometer (FIFI) provides linear fringes. However, the fringe shape is very sensitive to the incident angular distribution (see Section 3.A) and does require collimated light, which complicates range-dependent measurements in the near field (50–300 m). This is not the case with field-widened Michelson and Mach–Zehnder interferometers. The QMZ and FIMZ techniques have very low penalty factors and do not require knowledge of the scattering ratio. It can be seen that the penalty factor for the FIMI is about two times the penalty factor for the FIMZ. This is because half of the light is back reflected [factor F, Eq. (3)].

A possible option to decrease the FIMI penalty factor by a factor of two is to tilt the FIMI at a small angle with respect to

**Table 1.    Penalty Factors for Wind Speed Measurement**

| Technique | $\kappa_{\text{VLOS}}$ | Technique | $\kappa_{\text{VLOS}}$ |
|---|---|---|---|
| DFP | 2.4 [56] | DMZ | 1.65 [27] |
| FIFP | 3.1 [57], 2–4 [58] | QMZ | 2.3 [27] |
| FIMI | 4.4 [33] | FIMZ | 2.3 [28] |

the incident light and to image the back-reflected interference fringe on a second detector.

The design of such a tilted FWFIMI is described in Sections 3.B and 3.C.

## 3. DESIGN OF A MONOLITHIC FWFIMI

### A. Lidar Geometry Requirements

Before we describe the design of an FWFIMI, in this section, we take a closer look at the geometric requirements. Range-resolved detection in the near-field requires a large FOV of the telescope for full overlap at all ranges in order to maximize the received signal. Furthermore, pointing stability of the laser beam is required to ensure a constant illumination function of the FIMI.

In a monostatic coaxial free-beam setup, where the laser beam, telescope, interferometer, and detector are on the same optical axis, the range dependence of the illumination function manifests mainly in a varying angular distribution and width of the illumination, due to the shift of the focus of the telescope. A bistatic setup complicates things, because it causes an additional range-dependent lateral shift of the illumination function. We expect that range-dependent calibration would be required to account for the range dependence of the illumination function.

The pointing stability and lateral shift of the illumination function in a free-beam setup have to be monitored, such that the bias on wind speed measurements can be corrected. During ALADIN Airborne Demonstrator (A2D) [60] measurements (DFP method), for instance, an unconsidered noise of the vertical alignment angle in the atmosphere of 1 µrad (10 µrad at the DFP) would cause an error in the wind speed determination of 0.4 m/s [61].

As we propose in Section 4, the illumination function can also be stabilized in a fiber-coupled setup by scrambling with fibers using a two-lens-optical scrambler. The large FOV is maintained using multimode fibers with large core diameters.

In all those cases, the large required FOV (large beam etendue) causes an angular distribution, which has to be compensated for by field widening.

The purpose of the following section is to demonstrate the consequences of the above-stated requirements in the case of a Newton telescope with a 15 cm diameter and a near-field distance range of 50–200 m.

We assume a coaxial arrangement of the laser beam with divergence $\Theta$ of 150 µrad (full width) and a collimated laser beam waist $w(R)$ of 13 mm at $R = 0$ and the telescope. Mirror M1 is used to send the laser beam into the atmosphere. If mirror M1 is unstable with respect to the rotation around the x-axis, the laser beam can be misaligned by an angle $\delta$ and the laser spot at distance $R$ is shifted by a distance $y(R)$. Lens L3 is used to quasi-collimate the light received by the Newton telescope. A field diaphragm can be inserted at position a to limit the FOV of the telescope. In a free-beam setup, an interferometer could be installed at position b. In a fiber-coupled setup, the lens Cl1 is used to couple the light into a multimode fiber at position c.

The overlap function $\xi(R) = A_{\text{eff}}/A_r$ describes losses of light collection efficiency due to imperfect coincidence between the FOV and the laser beam or due to obstacles inside the telescope, where $A_r$ is the telescope area and $A_{\text{eff}}$ is the effective telescope area. The total overlap distance $R_{\min}$ is reached when $\xi(R_{\min}) = 1$. For $R_{\min} = 40$ m, the respective necessary FOV is obtained from the equations of Stelmaszczyk et al. for the overlap function without obstruction by the secondary telescope mirror [62]. An FOV (full width) of 4 mrad is thus required. The FOV is limited by the diameter of the field diaphragm ($d_s$) in the focus of the telescope, i.e., FOV $= d_s/f_t$, where $f_t$ is the focal length of the telescope primary mirror for an infinitely distant light source. The light beam direction angular distribution with maximum angle $\sigma$ before the primary mirror is magnified due to the angular magnification $\gamma$ of the telescope, and $\gamma = d_t/d_c = f_t/f_c = \tan(\sigma')/\tan(\sigma)$. Here, $f_c$ is the focal length of the collimating (ocular) lens, and $d_c$ is the diameter of the "collimated" beam behind the collimating lens. $\sigma$ and $\sigma'$ are the angles before the primary mirror and after the collimating lens. In our example, $f_t$ is 750 mm, $f_c$ is 60 mm, $d_c$ is 11.4 mm, and thus, $\gamma$ is 13.2. The angular distribution at the interferometer is a consequence of the shift of the focal spot position of the telescope as a function of the range ($R$). Because the distance between the collimating lens and the focal spot is fixed, as is $f_c$, ideal collimation is only possible for exactly one value of $R$. The collimating lens (CL) is fixed such that, for example, the light coming from $R = 90$ m is collimated, because light shall be collected from a close distance. To model this, three point sources (1, 2, and 3) are defined at distance $R$ in front of the telescope; they are located in the middle and at the edges of the laser illumination area with diameter $w(R)$. The layout is shown in Fig. 2(i). The telescope tubus opening is defined as the entrance pupil. The marginal rays of each point source are traced, and the direction cosines are determined at a surface b behind the collimating lens. All ray-tracing simulations are carried out with the software ZEMAX. The points a, b, and c mark the positions of the focus of the telescope, the location of the FIMI (free-beam setup), and the location of the entrance of the scrambling fiber (fiber-coupled setup), respectively.

The maximum angles $\sigma'$ (marginal ray angle) are evaluated as a function of the distance $R$, at position $b$, for the three point sources (1: dashed, 2: continuous, and 3: dotted line) in Fig. 2(ii).

The angular distribution is range dependent and varies between $\pm 2$ and $\pm 17$ mrad (green lines). At $R = 50$ m, the anglular distribution is $\pm 12$ mrad. These angular distributions require so-called field widening. Fluctuating values of the horizontal laser beam allignment tilt angle $\delta$ can be caused by mechanical instabilities (e.g., mirror M1). In this case (blue, $\delta = 0.1$ mrad), the angular distribution gets an offset of $\gamma \times \delta = 1.32$ mrad.

For these angular distributions of the incident light, the fringe shape stability of a FIFI and a FIMI with and without field widening can be compared. Following the description by Novak et al. for a FIFI [63], multiple plane waves are propagated along their propagation vectors. The plane waves are reflected and refracted in the interferometers. Their phases are recorded and they are superimposed in a plane. The intensities are summed up along the direction of the fringes. In case of the FIMI, the beam splitter is completely omitted. The
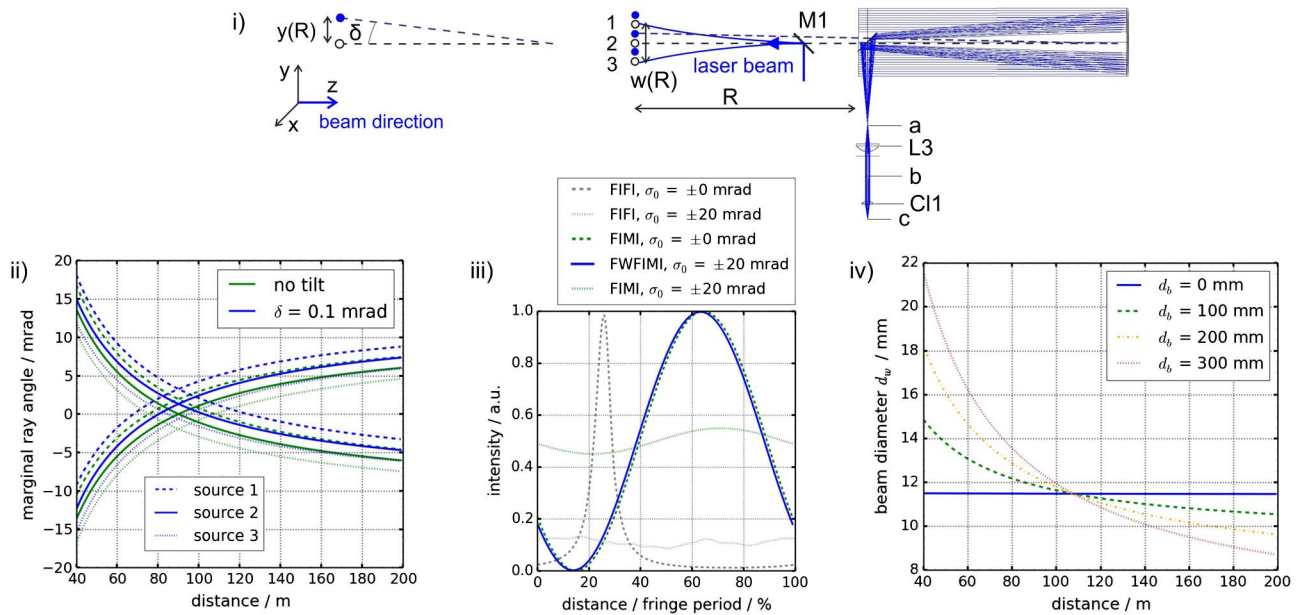
**Fig. 2.** (i) Ray-tracing layout of a Newton telescope with three point sources (1,2,3) at distance $R$ and planes a, b, and c. (ii) Marginal ray angles as a function of $R$ without tilt ($\delta = 0$, green) and with a tilt of the laser beam ($\delta = 0.1$ mrad, blue). (iii) Angular sensitivity of fringe shapes of a fringe-imaging Fizeau interferometer and of a fringe-imaging Michelson interferometer, the latter with and without field widening for collimated light and incidence angle distributions of $\sigma_0 = \pm 20$ mrad. For better visibility, the fringes for angular distributed light have been shifted in the x-direction. (iv) Illumination beam diameter as a function of distance $R$ for different distances $d_b$.

obtained interference fringe shapes are shown in Fig. 2(iii) for a FIFI and for a FIMI without and with field widening (FWFIMI) for collimated light and for light with incidence angles $\sigma_0$ of $\pm 20$ mrad. The illumination diameter $d_w$ is 10 mm. The net inclination angle is 17.75 µrad, such that one fringe period is imaged. The FIFI mirrors have exemplary values of reflectivity of 80% and a separation of 7.5 mm. For the FIMI and FWFIMI, the parameters given in Section 3.C are used.

In case of the FIFI, the fringe shape is strongly dependent on the angular distribution. The finesse and the contrast decrease rapidly with increasing $\sigma'$. No fringe can be obtained for $\sigma_0 = \pm 20$ mrad. For the uncompensated FIMI, the contrast decreases likewise. The FWFIMI is insensitive to the angular distribution (blue line).

The field widening only compensates the angular distribution and not the offset in the position or tilt of the illuminating beam. The actual shift of the illumination on the detector depends on the imaging optics used (e.g., Section 4). This shift of illumination would introduce large errors into the determined wind speed. The tilt $\delta$ results in a transversal shift at the position of the focus of the telescope primary mirror (a) and after the collimating lens (b). If the FIMI is positioned in $b$, the illumination of the FIMI depends on $R$ and $\delta$.

The offset in the $y$-direction at surface b, due to the tilt $\delta$, is $\tan(\gamma\delta)d_b$, where $d_b$ is the distance between the focal plane of the collimating lens and surface b. The interference fringe is displaced on the detector by at least $\Delta y_d = \tan(\gamma\delta)(d_b + d_z)$. Here, $d_z$ is the distance between the entrance of the FIMI and the detector. The geometry constraints of the setup (Section 4) impede small values of $d_z$. Assuming one fringe period is imaged ($N_p = 1$) with $d_w = 10$ mm, $d_b = 20$ cm, and $d_z = 14$ cm

according to Eqs. (3) and (4) of Section 2.B, a tilt of $\delta = 1$ µrad causes an estimated positional fringe shift $\Delta y_d$ of 4.5 µm on the detector. The values of $d_b$, $d_z$, and $d_w$ can be slightly different in a real setup. Seeing that the phase sensitivity $S$ defined in Section 2.B is 3.3 mrad/(m/s) for an FSR of 10.7 GHz and a wavelength of 355 nm, we see that a wind speed of 1 m/s gives a shift of 1/1900 of the imaged fringe period width $d_w$. Comparing this to the $y_d = 1/2228 \times d_w$, a bias of 0.9 m/s is estimated. Two lenses of equal focal length $f$ at distance $2f$ can be used to image the focal plane of the collimating lens on the entrance of the FIMI (i.e., $d_b = 0$). In this case, the estimated bias for $\delta = 1$ µrad is 0.4 ms$^{-1}$. This order of magnitude of bias could severely degrade the measurement performance, as can be seen with respect to the results and discussion in Section 5.

The range dependence of the illumination manifests in a varying beam diameter $d_w$ [Fig. 2(iv)], which could be accounted for by range-dependent calibration. A configuration with 2 lenses to image the focal plane of the collimating lens on the entrance of the FIMI also minimizes this range dependence (i.e., $d_b = 0$). Another way to reduce the range dependence of $d_w$ is the already-mentioned fiber-coupled setup. In this case, the fiber core diameter determines the angular distribution of the light in the far field behind the fiber, e.g., $\sigma_0 = \pm 16$ mrad in case of a fiber core diameter of 6.0 µm. Accordingly, the field-widening compensation is necessary in the fiber-coupled case, as well.

The design principles of a monolithic FWFIMI are described in the next sections.

**B. Fringe Imaging**

The monolithic FIMI is meant to produce linear fringes, and therefore, the mirrors of the two arms are inclined with respect

to each other. Exactly one fringe period ($N_p = 1$) shall be imaged on the detector to maximize both the modulation depth of the fringes and the number of pixels per fringe period. The width of the illuminating beam $d_w$ shall be 10 mm. The wavelength of the laser ($\lambda_L$) is 354.84 nm. The ideal net inclination angle $\theta$ between the mirrors is thus 17.74 µrad.

## C. Field Widening

The term field widening (FW) refers to the ability of an interferometer to accept angular distributed light without a reduction in the fringe contrast, i.e., an FWFIMI is compensated for a larger beam étendue. Field widening makes the OPD roughly independent of the incident angle ($\sigma_0$). The FW compensation requires a special solution for the refractive indices and lengths of the arms of the Michelson interferometer. The compensation can only be achieved for a fixed FSR at a selected tilt angle ($\theta_t$) with respect to the incident light. In Section 2, an ideal FSR of 10.7 GHz for wind speed measurements was determined. In a dispersion-free interferometer, the optical path difference (OPD$_{opt}$) is thus 28 mm. In order to achieve field widening, the refractive indices of arm one ($n_1$) and arm two ($n_2$) have to be different. This requires in general the use of at least two different optical glasses for the interferometer arms or one arm made of air and one of glass.

We selected the second option because it offers an important refractive index difference $\Delta n$, which minimizes the lengths of the interferometer arms, reduces temperature sensitivity [64], and leaves the option of pressure tuning the fringe position. Apart from the required spacers, it keeps the instrument simple.

Figure 3 shows a schematic of our monolithic FIMI illuminated at a tilt angle ($\theta_t$) of 2°.

$n_1$, $n_2$, $d_1$, and $d_2$ are the absolute refractive indices and lengths of the interferometer arms. $n_0 = n_a$ is the refractive index of air. $\sigma_0$, $\sigma_1$, and $\sigma_2$ are the angles of incidence and refraction in the respective media. $\theta_t$ is the mean incident angle of the divergent light beam with angular distribution $\sigma_0 = \pm16$ mrad (full width). In the scheme, a perfectly collimated beam is drawn for simplicity. In the following considerations, the cubic non-polarizing beam splitter is omitted due to symmetry.

The optical path difference OPD can be expressed as a function of incident angle in the following way:

$$\text{OPD} = 2n_1 d_1 \cos(\sigma_1) - n_2 d_2 (\cos(\sigma_2) + \cos(\sigma_2 \pm 2\theta)). \quad \textbf{(7)}$$
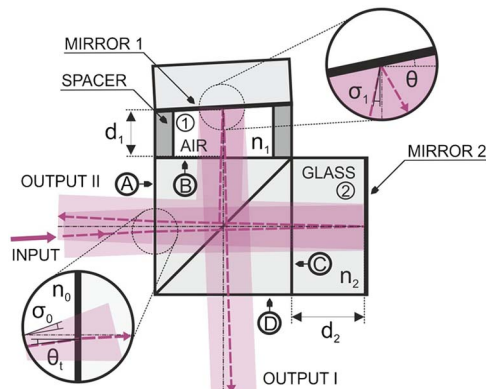


**Fig. 3.** Monolithic fringe-imaging Michelson interferometer (FWFIMI) tilted by 2° with air arm (1) and glass arm (2).

Seeing that $\cos((2\theta)) = 1 - 1.6 \times 10^{-10}$, we can set $\theta$ equal to 0. By using Snell's law, $n_0 \sin(\sigma_0) = n_1 \sin(\sigma_1) = n_2 \sin(\sigma_2)$, using $\cos(\sigma) = (1 - \sin^2(\sigma))^{1/2}$, and expanding $\sin(\sigma_0)$, one obtains the familiar expressions for the OPD [65]:

$$\text{OPD}(\sigma_0) = 2n_1 d_1 \sqrt{1 - \frac{\sin^2(\sigma_0)}{n_1^2}} - 2n_2 d_2 \sqrt{1 - \frac{\sin^2(\sigma_0)}{n_2^2}}, \quad \textbf{(8)}$$

$$\text{OPD}(\sigma_0) = 2(n_1 d_1 - n_2 d_2) - \sin^2(\sigma_0)\left(\frac{d_1}{n_1} - \frac{d_2}{n_2}\right) - O(\sigma_0^4) - \cdots$$
$$\textbf{(9)}$$

The first term is the OPD at the central incident angle $\theta_t = 0$ and is called the fixed optical path difference (OPD$_0$).

For field widening, the second-order term is set to zero (field-widening condition),

$$w = \frac{d_1}{n_1} - \frac{d_2}{n_2} = 0. \quad \textbf{(10)}$$

If the Michelson interferometer is tilted by the tilt angle $\theta_t$ with respect to the incident light, the expressions for OPD$_0$ and $w$ are [66]

$$\text{OPD}_0(\theta_t) = 2\left[ n_1 d_1 \sqrt{1 - \frac{\sin^2(\theta_t)}{n_1^2}} - n_2 d_2 \sqrt{1 - \frac{\sin^2(\theta_t)}{n_2^2}} \right], \quad \textbf{(11)}$$

$$w(\theta_t) = \frac{d_1}{\sqrt{n_1^2 - \sin^2(\theta_t)}} - \frac{d_2}{\sqrt{n_2^2 - \sin^2(\theta_t)}}. \quad \textbf{(12)}$$

In order to determine the optimal arm lengths $d_{1opt}$ and $d_{2opt}$ for field widening, this system of equations [Eqs. (11) and (12)] has to be solved, where $\text{OPD}_0(\theta_t) = \text{OPD}_{opt}$ and $w(\theta_t) = 0$. We choose to optimize the arm lengths for a tilt angle $\theta_t$ of 2°. This allows for the option of a second detector in back reflection (output II, Fig. 3). In this way, the efficiency of the Michelson interferometer could be nearly doubled ($\kappa_{VLOS} = 2.2$, compare to Table 1). The interference pattern of output II is shifted by $2(\delta_T + \delta_R) = \pi$ with respect to output I, where $\delta_T$ and $\delta_R$ are the phase shifts of transmittance and reflectance of the beam splitter.

The preferred glass material is fused silica (FS), because of its high transmission in the UV. The refractive index of the FS glass $n_{g_r}$ at wavelength $\lambda$ [µm] relative to air at $T_0$ and $p_0$ is calculated with the Sellmeyer equation [67],

$$n_{g_r}(\lambda) = \sqrt{1 + B_1 \frac{\lambda^2}{\lambda^2 - C_1} + B_2 \frac{\lambda^2}{\lambda^2 - C_2} + B_3 \frac{\lambda^2}{\lambda^2 - C_3}}. \quad \textbf{(13)}$$

Here, $B_1$, $B_2$, $B_3$, $C_1$, $C_2$, and $C_3$ are the Sellmeyer coefficients. In Eqs. (11) and (12) $n_2$ is equal to the absolute refractive index of glass $n_{g_a}(\lambda_L) = n_{g_r}(\lambda_L) \cdot n_a$. See Eq. (17) for the calculation of the absolute refractive index of air ($n_a$) at $T_0$. $n_1$ is equal to $n_a$ at the reference temperature ($T_0$) of 22 °C. The field-widening compensation can only be done for one wavelength. By setting $\text{OPD}_{opt} = 28$ mm and solving the system of equations in Eqs. (11) and (12), the optimal arm lengths are obtained, neglecting dispersion.

The wavelength dispersion of the glass arm, modifying the FSR, has to be considered. The OPD as a function of the wavelength is calculated by inserting Eq. (13) into Eq. (11). OPD ($\lambda$) is put into the Michelson transmission function Eq. (3).
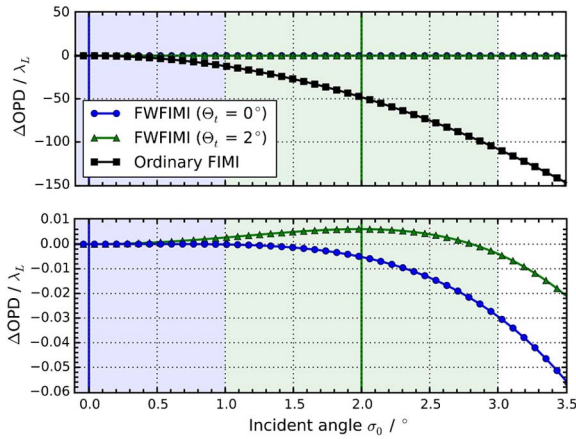
**Fig. 4.** OPD change in wavelengths as a function of incident angle for FWFIMI field widened for $\theta_t = 0°$ and 2° and uncompensated FIMI. Vertical lines mark the respective tilt angle ($\theta_t$).

The correct values of $d_{1opt}$ and $d_{2opt}$ are determined by an iterative optimization process. $\mathrm{OPD}_{opt}$ is varied until one fringe period exactly spans 10.7 GHz.

The change of OPD as a function of the incident angle $\Delta\mathrm{OPD}(\sigma_0) = \mathrm{OPD}_0 - \mathrm{OPD}(\sigma_0)$ is a measure of the quality of the field compensation. Figure 4 shows $\Delta\mathrm{OPD}(\sigma_0)$ in wavelengths ($\lambda = \lambda_L$) for FIMIs field widened for $\theta_t$ values of 0° and 2° (vertical lines mark the mean incidence angle) and for the case of an ordinary Michelson interferometer with the same FSR (10.7 GHz).

For the FWFIMIs, the variations of the OPD within one degree (17.4 mrad) of less than $0.003\lambda_L$ for $\theta_t = 0°$ and about $0.01\lambda_L$ for $\theta_t = 2°$ are very small in comparison to the $15\lambda_L$ in case of the ordinary MI for $\theta_t = 0°$. Angular distributions of $\pm 16$ mrad (see Section 3.A) are thus compensated for by field widening.

## D. Temperature Compensation

The FWFIMI can be more easily temperature stabilized at elevated operational temperatures. We are interested in temperature-induced shifts of the fringe position during the measurements, i.e., during the time needed for digital averaging over several pulses. The temperature tuning rate $R_T$ is the shift of the fringe spectral position in Hz per Kelvin. Low values of $R_T$ minimize temperature-induced biases of $u_r$. $R_T$ is mainly determined by the spacer material used in the air arm. The spacer material should be optimized for small temperature tuning. Our goal in this section is to find such a spacer material.

Thermal compensation requires the derivative of the fixed OPD with respect to temperature being close to zero,

$$\frac{\partial\mathrm{OPD}_0(\theta_t)}{\partial T} = 0$$

$$= 2\left[\alpha_1 d_1 (n_1^2 - \sin^2(\theta_t))^{\frac{1}{2}} + \beta_1 n_1 d_1 (n_1^2 - \sin^2(\theta_t))^{-\frac{1}{2}}\right]$$
$$- 2\left[\alpha_2 d_2 (n_2^2 - \sin^2(\theta_t))^{\frac{1}{2}} + \beta_2 n_2 d_2 (n_2^2 - \sin^2(\theta_t))^{-\frac{1}{2}}\right]. \quad \textbf{(14)}$$

Here, $\alpha_k = (1/d_k)\partial d_k/\partial T$ is the coefficient of the linear thermal expansion (CTE) of the material $k$, and $\beta_k = \partial n_k/\partial T$ is

the thermal coefficient of the refractive index. $n_1$ and $n_2$ are the absolute refractive indices of air and glass. This condition [Eq. (14)] can be fulfilled by choosing a material for the air arm spacer with the right CTE ($\alpha_1$). The ideal value of $\alpha_1$ is determined in the following. For the calculations, we assume the values of $d_{1opt}$ and $d_{2opt}$ are those determined in Section 2.C. The CTE of fused silica ($\alpha_2$) is $0.51 \cdot 10^{-6}$ K$^{-1}$.

The thermal coefficient of fused silica ($\beta_2$) may be calculated with the derivative of the Sellmeyer equation with respect to the temperature [68],

$$\frac{dn_{g_a}(\lambda_L, T)}{dT} = \frac{n_2^2(\lambda_L, T_0) - 1}{2n_2(\lambda_L, T_0)}\left(D_0 + 2D_1\Delta T\right.$$
$$\left. + 3D_2\Delta T^2 + \frac{E_0 + 2E_1\Delta T}{\lambda_L^2 - \lambda_{TK}^2}\right). \quad \textbf{(15)}$$

Here, $n_2(\lambda_L, T_0)$ is the refractive index of the glass at the laser wavelength $\lambda_L$ in µm, obtained with the Sellmeyer equation at the reference temperature ($T_0$) of 22 °C. $\Delta T = T - T_0$ is the temperature difference versus $T_0$. $T$ is the temperature in °C. $D_0$, $D_1$, $D_2$, $E_0$, $E_1$, and $\lambda_{TK}$ are the thermal dispersion coefficients of the glass. The change of the absolute refractive index $\Delta n_{g_a}(\lambda_L, \Delta T)$ may be calculated by integrating Eq. (15).

The absolute refractive index of the glass at temperature $T$ is $n_{g_a}(\lambda_L, T) = n_{g_a}(\lambda_L, T_0) + \Delta n_{g_a}(\lambda_L, \Delta T)$.

The thermal coefficient of air ($\beta_1$) and the refractive index of air $n_a(\lambda_L, T, P)$ are calculated by [68]

$$\beta_1 = \frac{dn_a(\lambda_L, T)}{dT} = -0.00367 \times \frac{n_a(\lambda_L, T, p) - 1}{1 + 0.00367\left(\frac{1}{°C}\right)T}, \quad \textbf{(16)}$$

$$n_a(\lambda_L, T, p) = 1 + \frac{n_a(\lambda_L, 15°C, p_0) - 1}{1 + 3.4785 \times 10^{-3}\frac{1}{°C}(T - 15°C)}\frac{p}{p_0}\lambda_L^2, \quad \textbf{(17)}$$

where $p_0 = 0.101325 \times 10^6$ Pa is the standard pressure at 20°C. $n_a(\lambda_L, T, p)$ is the absolute refractive index of air at the air pressure $p$ and at the temperature $T$ in °C. $\lambda_L$ is the laser wavelength in µm.

Seeing that $n_1/\sqrt{n_1^2 - \sin^2(2°)}$ is 1.0003, we can set $\theta_t$ equal to 0° in Eq. (14) in the following for simplicity. Two variants of temperature tuning are possible. The first is temperature tuning with a constant air density ("TTCD", i.e., $\beta_1 = 0$), as in the case of isochoric heating, when the FIMI is enclosed in a sealed container. We can set $n_a = 1$, from which it follows that $n_{g_a} = n_{g_r}$. The second is temperature tuning at a constant air pressure ("TTCP"). TTCP occurs when the container is not sealed. By inserting the field-widening equation into the temperature compensation condition, we obtain, in the cases of TTCD and TTCP, the following results for the optimized CTE values of the spacers for CD and CP, respectively:

$$\alpha_{1CD} = n_{g_r}^2\left(\frac{1}{n_{g_r}} + \alpha_2\right), \quad \textbf{(18)}$$

$$\alpha_{1CP} = \frac{n_{g_a}(T_{op})}{(n_a(T_{op}))^2} \times \beta_2 + \frac{(n_{g_a}(T_{op}))^2}{(n_a(T_{op}))^2} \times \alpha_2 - \frac{1}{n_1} \times \beta_1. \quad \textbf{(19)}$$

The ideal CTE values of the spacers for zero temperature tuning in our case are $\alpha_{1\mathrm{CD}} = 16.4$ ppm/K and $\alpha_{1\mathrm{CP}} = 17.3$ ppm/K.

To evaluate the rate for different values of the spacers' CTEs, one can use the absolute refractive indices of glass and air and the arm lengths $d_k(T) = d_k(T_0)(\alpha_k \Delta T + 1)$ to determine the fixed OPD values at the temperatures $T_1$ and $T_2$. These fixed OPD values are then used to calculate the Michelson transmission functions at $T_1$ and $T_2$. The transmission function [Eq. (3)] is evaluated over the frequency range of one FSR for $T_1 = 40°C$ and $T_2 = 41°C$ for TTCD and TTCP for different values of the spacers' CTEs. In each case, the temperature tuning rate is determined from the shift between the transmission functions at $T_1$ and $T_2$. The temperature tuning rate is plotted in Fig. 5(a) as a function of the CTEs of the spacers for both TTCD and TTCP.

The respective ideal CTE values $\alpha_{1\mathrm{CD}}$ and $\alpha_{1\mathrm{CP}}$ are highlighted (dotted lines). If we extrapolate the trend to 0.51 ppm/K, the temperature rate would be higher than one FSR. Making the spacers of the same material as the glass arm is therefore not an option. Copper ($\mathrm{CTE}_{\mathrm{Cu}} \approx 17$ ppm/K) and calcium fluoride ($\mathrm{CTE}_{\mathrm{CaF_2}} = 19$ ppm/K) are suitable materials. Mahadevan *et al.* [69] used a copper ring spacer glued to a BK7 beam splitter with a UV cure epoxy. Stability issues and thermal drift were reported later and were explained with shear stresses due to the large CTE difference between copper and BK7 [70]. A concept applied by Harlander *et al.* [71] is to fabricate column spacers of calcium fluoride ($\mathrm{CaF_2}$) with relatively small cross sections in order to minimize the thermal stresses. The $\mathrm{CaF_2}$ can be glued to FS components with a UV cure epoxy.

Furthermore, the spacer columns can be fabricated as a composite of FS and $\mathrm{CaF_2}$. In this way, the net CTE of the spacers can be tuned by $\mathrm{CTE}_C = j \times \mathrm{CTE}_{\mathrm{FS}} + (1 - j) \times \mathrm{CTE}_{\mathrm{CaF_2}}$, where $j$ is the length fraction of glass in the composite. The glass part length $d_{\mathrm{FS}}$ is $j \times d_2$. Figure 5(a) shows $d_{\mathrm{FS}}$ as a function of $\mathrm{CTE}_C$.

The required CTE values ($\alpha_{1\mathrm{CD}}$, $\alpha_{1\mathrm{CP}}$) require a polished glass part thickness ($d_{\mathrm{FS}}$) smaller than 2 mm, which is hard to achieve. We select the TTCD tuning mode because it allows us to seal the Michelson compartment for protection and
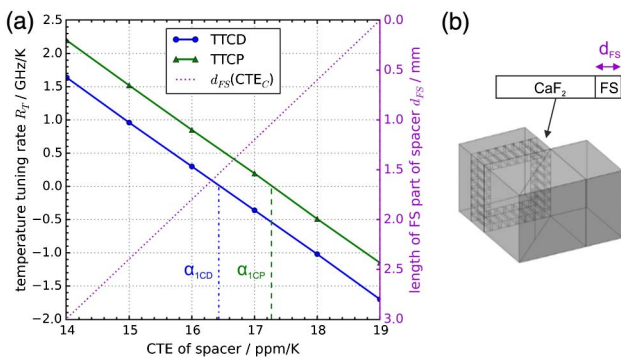
pressure tuning and because the tuned CTE value is closer to $\alpha_{1\mathrm{CD}}$. A three-dimensional model of such an interferometer can be seen in Fig. 5(b).

For the measurements, the interferometer will be heated up from the fabrication temperature (22°C) to the operation temperature (40°C) at a constant density. In the case of TTCD, $\beta_1$ is zero and $\alpha_1$ is assumed to be 15.5 ppm/K. The change of the air arm length $\Delta d_1$ for $\Delta T = 18$ K is 3.1 μm, while $\Delta d_2$ is 0.15 μm. The change of the arm lengths is compensated for by making the initial air arm length 3 μm shorter. One may ignore the thermal coefficient of the fused silica slice ($\beta_2$), which is a fair approximation. The change of the FSR over a temperature range of 20 K is smaller than 0.2%.

## E. Fabrication Tolerances

For a realistic evaluation of the expected performance, fabrication tolerances and their influence on the instrumental contrast $V$, and therefore on the performance, have to be considered. In the following, some of the important parameters of the FWFIMI are varied in order to visualize the significance of fabrication tolerances and their consequences.

### 1. Arm Lengths and Refractive Index Tolerances

At first, the influence of arm length tolerances on the instrumental contrast is considered. The OPD is calculated for a systematic variation of $d_1 + \Delta d_1$ and $d_2 + \Delta d_2$ in Eq. (8) for the angle-dependent OPD for different incident angles ($\sigma_i = \theta_t \pm 16$ mrad). The corresponding transmission functions are calculated using Eq. (3) for each configuration (pair of $d_1$ and $d_2$) at a temperature of 40°C. The transmission functions for different $\sigma_i$ are summed up to yield the global transmission function for the angular distribution. The contrast of the global fringe pattern is determined for each configuration. In the calculations, dispersion is neglected. The contrast is plotted in Figs. 6(a) and 6(b) as a function of $\Delta d_1$ and $\Delta d_2$ for $\theta_t = 2°$ and $\theta_t = 0°$.

In case of $\theta_t = 2°$ a tolerance for the arm lengths $\Delta d$ of $\pm 10$ μm (see white rectangle) may reduce the global fringe contrast in the worst case to 97%. A reduction of the tilt of the FWFIMI decreases the sensitivity of field widening to the arm length tolerances. For $\theta_t = 0°$, the contrast is always equal to 1 within $\pm 10$ μm. A reduction of the angular distribution $\sigma_i$ decreases the sensitivity as well. However, in Section 3.A we saw that a required FOV of 4 mrad results in a $\sigma_i$ on the order of $\pm 16$ mrad.

**Fig. 5.** (a) Temperature tuning rate for tuning modes: constant density (TTCD) and constant pressure (TTCP) as a function of the CTE of the spacer and according length of the FS part of a composite spacer made of silica and calcium fluoride. (b) Three-dimensional model of the FWFIMI with composite spacers in the air arm.
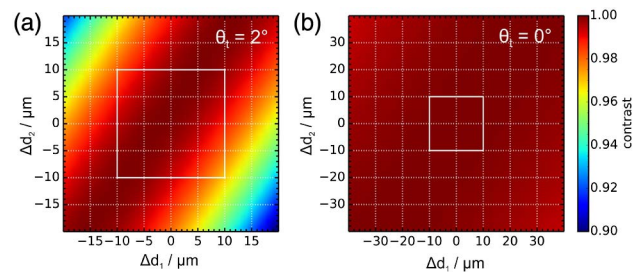
**Fig. 6.** Global contrast for angular distributed light incident on an FWFIMI, where the arm lengths $d_1$ and $d_2$ are varied around the ideal values for mean angles of incidence of $\theta_t = 2°$ (a) and $\theta_t = 0°$ (b). Tolerances are indicated by white squares.

Similar considerations can be done for the refractive index of the glass arm. It has a refractive index consistency of 1 part in 2000. The reduction of contrast due to such a variation of $n_g$ is less than 0.2%.

### 2. Coatings

The quality of the coatings applied to the interfaces of the FWFIMI determines the instrumental fringe contrast $V$ and the efficiency of the FWFIMI as well. We consider a beam splitter coating with a reflectivity of 50% ± 2% at 355 nm for s-polarized light at incident angles of 45° ± 2°. The term splitting ratio refers to the ratio of the luminous light intensity transmitted ($I_T = tI_0$) and reflected ($I_R = rI_0$) by the beam splitter coating. Here, $I_0 = E_0^2$ is the luminous light intensity of the input beam, and $t$ and $r$ are the intensity transmission and reflection coefficients of the beam splitter, where $t + r = 1$. The total intensity $I_{tot}$ at the FIMI mirrors, where the interference pattern is localized (see: Section 3.F.2.), can be written as

$$I_{tot} = |\sqrt{r}E_0 + \sqrt{t}E_0 \exp j\phi|^2 = I_0[1 + V_{BS}\cos(\phi)]. \quad (20)$$

Here, $\phi$ is the phase, and $V_{BS} = \sqrt{rt}$ is the maximum contrast due to the repartition of energy by the beam splitter in the two arms of the FIMI. In the case of $r = 0.52$ and $t = 0.48$, $V_{BS}$ amounts to 99.9%. The reflectance for p-polarized light is low (3–8%). For pure p-polarized light, $V_{BS}$ would be 34–54%. A polarizing element before the FIMI should guarantee that the incident light is s-polarized in order to ensure a high instrumental contrast.

The instrumental contrast depends, as well, on the anti-reflection (AR) coatings applied to the surfaces of the beam splitter. Due to imperfect AR coatings, the reflected signal will interfere with the primary signal and will be visible as a background due to the big intensity difference [72]. This can reduce the contrast. As a countermeasure, the surfaces A, B, and D (see Fig. 3) should be very well anti-reflection coated.

### 3. Mirror Inclination Angle

The net inclination angle between the mirrors ($\theta$, Fig. 3) is specified with 17.8±1 µrad. The corresponding number of imaged fringe periods ($N_p$) is 1 ± 0.06. In case of $N_p = 0.94$, the contrast is reduced by 2% because less than one fringe period is imaged. In this case, an increase of the illuminating beam diameter $d_w$ to 10.6 mm would correct $N_p$ back to one.

### 4. Net Surface Accuracy

The fringe shape is sensitive to deviations of the net contour from planarity. We consider the case where this deviation is in the form of a radial curvature, an assumed worst case. The effect on the fringe shape is modeled with a non-sequential ray trace in ZEMAX. According to ISO 10110, contour accuracy is given for a test wavelength $\lambda$ of 633 nm. We consider here surface errors $S_E$ of infinity, 20, and 10. The surface sag is then sag $= 0.00063$ mm/$S_E$. The radius of curvature is $R(\text{sag}) = (0.25d_C^2 + \text{sag}^2)/(2\text{sag})$, where $d_C = 19$ mm is the clear aperture of the FWFIMI. Figures 7(a) and 7(b) show the fringe shapes obtained by coherent raytracing with a collimated, quadratic-shaped, uniform illumination of wavelength $\lambda_L = 354.84$ nm and $d_w = 10$ mm, through an FIMI, where
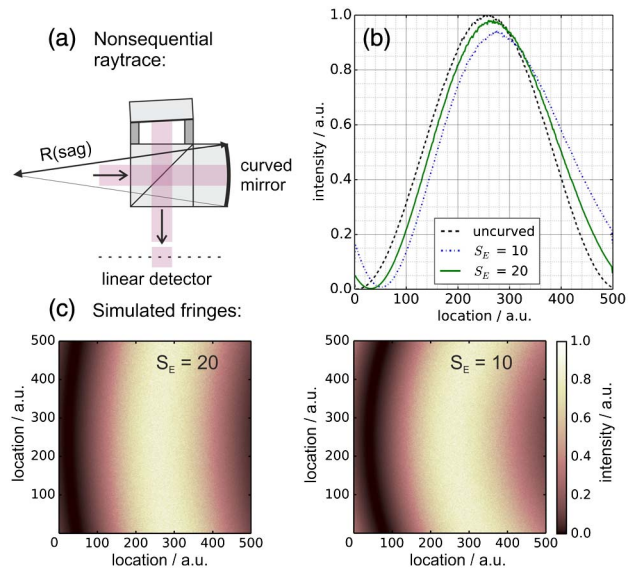


**Fig. 7.** Effect of net surface radial curvature on fringe shape (a) scheme of the non-sequential ray trace. (b) Integrated fringe shapes of an ideal uncurved fringe ($S_E = \infty$) and of the simulated fringes (c) for radial surface errors of $S_E = 20$ (left) and $S_E = 10$ (right).

the net radius of curvature of the mirrors is $R(\text{sag})$. The final shape of the fringe on a linear detector is obtained by the summation of all the pixels along the y-direction [Fig. 7(c)]. The y-axis is normalized to the intensity of the planar (uncurved) case.

As the net surface curvature increases, the fringe is curved more and more. Its summation in the y-direction results in an asymmetrical (skewed) fringe with reduced contrast. In the case of $S_E = 10$, the contrast is reduced by 6%. In case of $S_E = 20$, the reduction of the contrast is 2%. In reality, surface irregularities depend on the manufacturing process and may be random and far from radial. The actual fringe shape has to be measured, and the fitted model of the evaluation process should be adapted.

### F. Further Aspects

#### 1. Illumination Function

The above simulations were carried out with a quadratic cross section of the illuminating beam. Now we consider non-uniform cross sections, e.g., a round cross section. If offsets in temperature, wavelength, pressure, or speed of the measurement platform are large enough, the fringe is shifted more and more from center position to the edge of the illuminating disk. Less light traverses the FIMI at locations where the condition for maxima is fulfilled. A change of the integrated fringe shape is the result. This effect is not observed with a quadratic beam cross section. For illustration, the same simulation as in Section 3.E.4. is used with $S_E = \infty$ to generate fringe patterns for different wavelengths stepped by $\approx 1/10$ of the FSR. A homogeneous, collimated light beam with a uniform intensity distribution is considered. The resulting fringes are plotted for a round and a quadratic illumination shape in Figs. 8(a) and 8(b).

The quadratic aperture has the drawback that part of the light (20–30%) is blocked because the initial beam shape is round. In a second step, the central part of the beam cross
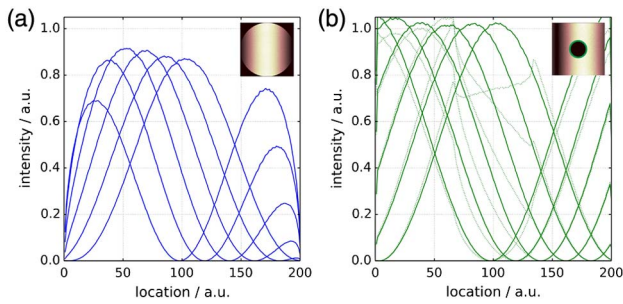
**Fig. 8.** Integrated interference fringe shape shifted within round (a) and quadratic (b) illumination and for an additional central obscuration (black circle, dotted lines).
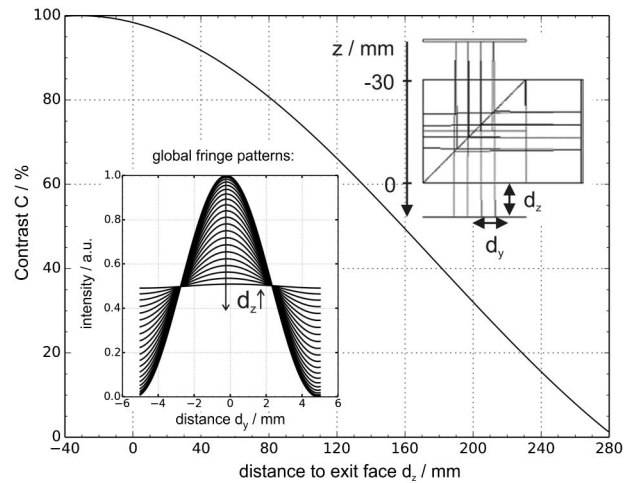


**Fig. 9.** Global fringe contrast as a function of the distance ($d_z$) from the exit face of the FWFIMI. Inset: Global fringe patterns for increasing values of $d_z$ and ray-tracing layout of the FWFIMI used for the simulations.

section is blocked (as marked by the black circle), as in the case of an obscuration by the secondary mirror of a Newton telescope. In this case, the fringe shapes become complicated (see dotted lines). Furthermore, the illumination is not uniform (flat top) in reality, due to the laser profile (e.g., a deformed $TEM_{00}$), due to the transmission through optical fibers or due to the obstruction by a telescope spider, for instance. The lower signal-to-noise ratio at high intensity values is an artifact of the coherent ray tracing in ZEMAX and is of no importance here.

In any case, the illumination function (i.e., the intensity distribution at the entrance of the FWFIMI) is very specific for the optics used, and it has to be characterized and has to be included in the final evaluation process. In Section 5 a quadratic cross section is considered, which facilitates access to output II.

### 2. Fringe Localization

Until now, we only considered the etendue of the illumination in terms of field widening, but not for fringe-imaging simulations. In reality, the illumination can be viewed as an extended disk made up of incoherent point sources (plane waves after collimation). Each point source produces a "non-localized" fringe pattern, where the visibility (contrast) is one everywhere and only depends on the relative intensities of the two waves that are made to interfere. The actual fringe pattern is the incoherent superposition of these elementary "non-localized" fringe patterns. The mutual displacement between the patterns and therefore the visibility of the global fringe pattern is dependent on the location of the imaging plane (because of the beam divergence) and may vary between 0 and 1. Such fringes are called "localized." An analytical description of fringe localization for the case of an FIMI is given by Fortunato [73].

Here, a more practical approach is used. Simulations of fringe localization are carried out in the sequential mode of ZEMAX. The layout of a monolithic FWFIMI can be seen in Fig. 9. The arm lengths and refractive index values are set to the ideal ones determined in Section 3. $\theta_t$ is set to zero. A number of rays with an angular distribution of $\pm 16$ mrad in the $x$- and $y$-directions are traced through the monolithic FWFIMI. The screen can be shifted in the $z$-direction towards the inclined mirror of the air arm ($d_z < 0$) and further away from the exit surface ($d_z > 0$). For every pair of rays, a pair of plane waves is constructed at the location of incidence on the imaging plane. The interference of each pair of plane waves is calculated on a two-dimensional grid in the $x$–$y$ plane at a

position $z$ to produce the "non-localized" fringe patterns. Their incoherent sum gives the global fringe patterns for different values of $d_z$.

Figure 9 shows global fringe pattern profiles (inset) for increasing values of $d_z$ and their contrast $C$ as a function of $d_z$.

$C$ contributes to the instrumental constrast $V$ [Eq. (3)], which is the product of all the contrast reducing contributions detailed in Section 3. The fringes are localized close to the mirrors of the FWFIMI. In order to maximize the visibility and the measurement performance, an imaging system is required that images the fringe localization plane on the detector plane located at positive values of $d_z$ outside the sealed compartment. Alternatively, the mirror inclinations of the FWFIMI and the mean incidence angle could be designed such that the localization plane is located at the detector plane. This solution, however, would increase the complexity of the FWFIMI and would reduce the flexibility of the instrument with respect to different detector types. Concepts for a possible receiver setup are proposed in the next section.

## 4. CONCEPT OF A RECEIVER SETUP

As pointed out in the sections above, the imaging Michelson interferometer for Doppler shift analysis may not be considered alone, but only by factoring in also the dedicated optics and detection systems. In this section, we propose some architecture suitable for the operation of the FWFIMI.

A possible schematic setup scheme for range-resolved detection in free-beam or fiber-coupled mode (see Section 3.A) is shown in Fig. 10(i).

A frequency-tripled Nd:YAG laser emits s-polarized pulses. The light scattered in the atmosphere at a 50–200 m distance may be collected with a telescope with a diameter suitable for the integration with an aircraft (e.g., 150–200 mm). Here m3, Tm1, and Tm2 refer to the laser steering mirror and to the primary and secondary telescope mirrors, respectively. The position of the ocular lens (L3) is set to collimate light from a
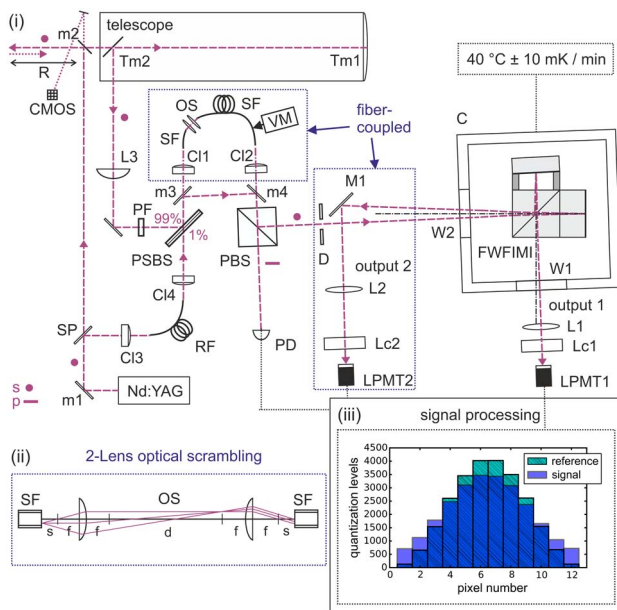
**Fig. 10.** (i) Receiver setup for the range-resolved measurement of wind speeds. Blue boxes mark components to be inserted for a fiber-coupled setup. (ii) Scheme of a two-lens optical scrambler with two aspheres of focal length f. (iii) Signal processing: light distributions on the linear detector (LPMT1) for reference and signal light (illumination function neglected).

distance of 90 m. The still mostly s-polarized light (considering the dominant Rayleigh scattering) passes through a narrow bandpass filter (PF) for background light suppression.

A small fraction of the laser light is split off as a reference beam with a splitter (SP) and is coupled into a single- or multi-mode fiber (RF) using the lens Cl3. The RF serves to delay the reference light with respect to the signal light. This light will be used to monitor the stability of the setup and as a reference for the determination of the Doppler shift.

The reference light and signal light are combined with the power-separating beam splitter PSBS, which reflects ≈99% of the signal light and transmits ≈1% of the reference light.

In a free-beam setup, the combined beam paths are directed over mirrors m3 and m4 into a polarizing beam splitter (PBS), such that only s-polarized light arrives at the FWFIMI. The unused part of the light may be temporally evaluated with a photodiode (PD) for monitoring purposes.

The FWFIMI may be fixed in a container (C) with fused silica glass windows (W1 and W2), which will be temperature stabilized to 40°C±10 mK/ min. In this way, the temperature tuning will be limited to less than 120 kHz/s ($\Delta u_r = 0.02$ ms$^{-1}$ s$^{-1}$). The lens L1 may be used in a 2f arrangement for 1:1 imaging of the localization plane onto the detector plane of output 1. The plano-convex cylindrical lens (Lc1) focuses the light in the direction parallel to the linear fringe on the linear detector, e.g., a linear photomultiplier tube array (LPMT1).

Output 2 is optional and is not needed for the setup to work. Due to the large dependence of the beam diameter on the distance (see Section 3.A), output 2 cannot be accessed in a free-beam setup.

A UV-sensitive CMOS camera can be used to monitor the stability of the laser beam alignment mirrors (m1, m2), which may be readjusted with a piezoelectric transducer. In this way, lateral instabilities of the illumination due to fluctuations of $\delta$ (as reported in Section 3.A) may be avoided.

Alternatively, a fiber-coupled setup may be used. In this case, mirrors m3 and m4 are omitted and, after the PSBS, the light is coupled into a large-core multimode fiber (SF). The SF serves several purposes. First, its core (quadratic, diameter of 6.0 μm) serves as a diaphragm, which limits the FOV of the telescope, in a magnitude which allows near-field range-resolved detection. Secondly, the SF's scrambling properties are intended to destroy the angular information of the light entering the telescope from different distances R and with oblique angles due to fluctuations of $\delta$. The scrambling properties may be improved using an optical scrambler (OS) [41]. Figure 10(ii) shows the scheme of a two-lens optical scrambler. Two AR-coated aspheric lenses of short focal lengths f are arranged with the proper distances s and d between two multimode fibers (SF), such that the fibers' near and far fields are exchanged between the fibers. Such a version with an SF will help to reduce the biases due to laser-telescope misalignments and drifts and may decrease the range-dependent imaging of the fringes (detailed in Section 3.A).

Due to the large beam divergence of ±16 mrad, output 2 is hard to access. A diaphragm with a quadratic opening (D) could be used to obtain a quadratic cross section (QBCS) of the illumination beam. D is necessary to increase the distance to the FIMI, such that the back-reflected light of output 2 can be collected with an inclined mirror (M1), while the cross-section diameter at the entrance of the FIMI is around 10 mm. The QBCS helps to make the fringe shape independent of the fringe position (see Fig. 8). The lenses L2 and Lc2 can be used to image the back-reflected fringe of output 2 on a second linear detector (LPMT2). This will nearly double the efficiency of the receiver.

A fiber-coupled setup has the disadvantage of more than 60% signal light losses due to coupling, absorption, the limited optical scrambler transmission efficiency, and due to depolarization within the multimode fiber. In order to limit the transmission losses, the SF should be kept short. The large core diameter imposes a divergence of ±16 mrad on the "collimated" light, which is, however, compensated by the FWFIMI. Furthermore, speckle patterns are generated due to the interference of multiple modes in the fibers. These speckle patterns make the illumination function erratic. One way to stabilize the illumination and reduce the speckle contrast is to use a vibration motor (VM) to move the SF in order to continuously generate random mechanical (and thus refractive) constraints for equilibrium mode distribution. With sufficient movement of the fiber, every laser pulse generates a new speckle pattern, and one can average over a multitude of pulses and obtain a stable light distribution on the linear detectors during the time of digital integration.

Figure 10(iii) shows exemplary light distributions for the reference and signal light on a linear detector array with 12 illuminated elements. Linear detectors could be Si-pin-photodiode arrays (QE≈50–60% in the UV, but without

internal amplification, which is problematic because of the low current levels obtained, which are likely to cause increased noise during current to voltage conversion, avalanche photodiode arrays (not available for UV wavelengths), or linear photomultiplier tube arrays (LPMT, QE≈40–45% in the UV). These linear detectors, used in analog detection mode, are fast enough for range-resolved detection with range gate lengths smaller than 20 m. The linear detectors exhibit pitches of 0.1–1 mm between the active elements. Neglecting the pitch between the detector elements, the modulation factor $V_{pix}$, due to the integration over the elements of a linear detector, has the tolerable value of sinc(1/P) (i.e., $V_{pix}$ = 99% for P = 12). $V_{pix}$ contributes to the instrumental contrast $V$.

All transmitted optical components (beam splitter, windows, lenses) should be AR coated for UV light to minimize losses and stray light.

In the next section, the performance of the proposed receiver setup is estimated using an end-to-end simulation.

## 5. ESTIMATION OF PERFORMANCE

In the following, an end-to-end simulation for an estimation of the performance of the receiver system, using output 1 [Fig. 10(i)] only, is described.

The simulation includes different transmitter properties, atmospheric backscattering conditions (Section 2.A), estimated losses of a receiver setup (Section 4), and an ideal instrument function of an FWFIMI (Section 2.B) to simulate the light distribution of the interference pattern imaged on the linear detector. Light distributions are generated for reference light and Doppler-shifted signal light. The illumination function, which is very specific for the receiver optics (see Section 3.F.1.), is not considered here. Speckle noise due to interference in the atmosphere and the interference of the optical fiber modes is modeled. For every detector element, analog detection noise (thermal noise, dark noise, shot noise, and solar background shot noise) and digitization are considered. The influence of crosstalk between neighboring detector elements is taken into consideration. Finally, the reference and signal light distributions, the interferometer's fringes, are processed with a fitting routine in order to determine the Doppler shift.

The amount of emitted light depends on the laser (transmitter system) being used. We assume different existing and proposed transmitter systems and consider their energy per pulse ($E_L$), their repetition rate ($R_L$), and power ($P_L$): WALES/ DELICAT [39] ($E_L$ = 80 mJ, $R_L$ = 100 Hz, $P_L$ = 8 W), the ESA MULTIPLY ($E_L$ = 1.5 mJ, $R_L$ = 4 kHz, $P_L$ = 6 W), AWIATOR [23] ($E_L$ = 0.17 mJ, $R_L$ = 18 kHz, $P_L$ = 3 W), and the hypothetic HYPO ($E_L$ = 8 mJ, $R_L$ = 1 kHz, $P_L$ = 8 W).

The total number of backscattered photons $n_p$ is calculated with the lidar equation [Eq. (2)] for different ranges, altitudes, and scattering ratios. Here, the factors $\eta_R$ = 20% and $\eta_T$ = 97% for the proposed setup are assumed. We estimate a total loss of signal photons before the detector of at least 92% in case of a fiber-coupled setup [see Fig. 10(i)] and a total loss including a linear PMT array of ≈97%. The backscattering coefficients $\beta_{Ray}$ and $\beta_{Mie}$ are obtained from a mid-latitude standard atmospheric model for different altitudes. $\beta_{Ray}$ and

$\beta_{Mie}$ are also used to calculate the light scattering spectra with the G3 model (see Section 2.A).

The spectra are convolved with the Michelson instrument function [Eq. (3)] using ideal values (determined in the Sections 2 and 3) to obtain the received spectrum and the received instrument function, i.e., the interference pattern ($I_F$). The instrumental interference contrast $V$ is estimated with 98%. All tolerances and all contrast-reducing imaging properties (Sections 3.E and 3.F) are assumed to be contained in $V$. Strictly linear fringes are assumed.

$I_F$ is normalized such that its integral is equal to the number of backscattered photons ($n_p$). $I_F$ is downsampled to simulate the detector elements of the linear detector [see Fig. 10(iii)]. The photocurrents per element are calculated from the number of photons.

In the next step, artificially produced noise is added on each detector element. An important cause of noise are speckle. Speckle are produced due to the interference of backscattered light from the atmosphere and interference of many propagation modes of reference light in the multimode delay fiber (RF) and signal light in the multimode scrambling fiber (SF). Speckle makes the illumination of the interferometer inhomogeneous and erratic. The intensity of speckle patterns obeys a negative exponential probability distribution function [74],

$$p_I(I) = 1/\langle I \rangle \exp(-I/\langle I \rangle). \qquad (21)$$

Here, $C = \sigma_I/\langle I \rangle$ is the speckle contrast. $\langle I \rangle$ is the mean value of the intensity illuminating the interferometer at a certain location. For coherent light, $\langle I \rangle$ is equal to the standard deviation $\sigma_I$. For partially coherent light, $C$ reduces to $1/\sqrt{M}$, here $M$ is the number of incoherently added speckle patterns. $M$ equals $M_a \times M_f$, where $M_a$ is the number of atmospheric speckle patterns, and $M_f$ is the number of fiber speckle patterns.

The illumination at the pupil of reception during the exposure time $t$ is composed of $M_a = \Delta R/d_{coh}$ speckle patterns. $d_{coh} = c\tau_{coh}/2$ is the coherence length, and $\tau_{coh}$ is the coherence time of the scattered light. For molecule scattering, $\tau_{coh} = 2/\pi\gamma$, where $\gamma = \sqrt{2}\sigma_{Ray}(T)$ is the half-width at 1/e of the scattering spectrum at the atmospheric temperature. For Rayleigh scattering, $\tau_{coh}$ is in the order of 0.3 ns. For Mie scattering, the coherence time is given by the pulse duration (7 ns).

In case of fiber-induced speckle, $C$ is reduced due to the mixing of the fiber modes during propagation, and $M_f$ depends on the vibration frequency of the vibration motor and the time of exposure of the detector, i.e., $t \approx 133$ ns ($\Delta R = 20$ m), and has to be determined experimentally. Due to this very short time $t$, we assume $M_f = 1$ for the simulations.

Every pulse is assumed to generate a new, arbitrary speckle pattern, due to the proposely changing distribution of scatterers in the scattering volume during flight from pulse to pulse (signal) and due to the vibration of the fibers (reference).

A simplified model is used to simulate the speckle patterns. An array of dimension 48 × 48 with a distribution according to Eq. (21) represents a coherent speckle pattern. The actual speckle grain size depends on the laser beam waist diameter, in our case, $w(R) > 20$ mm at $R = 50$ m (see Fig. 2), or on the multimode fiber core diameter [75]. The real speckle pattern properties have to be characterized for the used fibers.

The total speckle patterns for signal and reference are computed by the incoherent sum of $M_{\mathrm{Mie}}$ and $M_{\mathrm{Ray}}$ speckle patterns (signal) and $M_f$ speckle patterns (reference) for every laser pulse. $R_b$ is included by setting $\langle I \rangle$ in Eq. (21) equal to the number of backscattered Rayleigh and Mie photons.

The linear detector spatially integrates over the total speckle pattern. All rows of the total speckle patterns are summed up and are downsampled to simulate the integration by the linear detector. The downsampled speckle distribution is normalized to 1 and multiplied with the distribution of photons on the linear detector for every pulse before the detector noise is included.

The total noise current $i_n$ of every detector element in the analog detection mode is calculated with the standard equations for thermal noise current $i_T$, the shot noise current of the dark current $i_{\mathrm{SD}}$, of the photocurrent $i_{\mathrm{SL}}$, and the solar background light current $i_{\mathrm{SBG}}$ [76],

$$i_n = \sqrt{i_T^2 + i_{\mathrm{SD}}^2 + i_{\mathrm{SL}}^2 + i_{\mathrm{SBG}}^2}. \tag{22}$$

A solar background radiation power in the atmosphere of 300 W/m$^2$ sr μm is assumed. The FOV is set to 4 mrad (full width). The full width at half-maximum of the sunlight filter (PF) is assumed to be 0.5 nm, giving a transmission of 80%. $i_{\mathrm{SBG}}$ is in the order of a few μA.

The Poisson distribution of the noise can be approximated by a normal distribution because of the large magnitude of the detected photons. The signal-to-noise (amplitude) ratio for every detector element is $I_L / i_n$, where $I_L$ is the photocurrent of the respective detector element. Crosstalk between the detector elements is included using typical crosstalk ratios of PMT arrays of 3%, 0.6%, 0.2%, and 0.1% for the detector elements in a row next to a given detector element.

The analog-to-digital-converter (ADC) quantizes the analog signal. The resolution of the ADC is assumed to be 16 bits with an effective number of bits (ENOB) of 12 [see Fig. 10(iii)]. Simulations have shown that reduced ENOB values of 10 bits would not significantly decrease the signal-to-noise ratio for our application. ENOB values of 8 bits and 6 bits would decrease the performance. The reference photocurrent is for the optimum use of the quantization levels. The saturation level can be set to the expected maximum signal light current by the adjustment of the PMT gain. A less scientific implementation should automatically adapt the amplification to the varying altitude $h$ and scattering ratio $R_b$. In this case, the signal currents could be adjusted to a lower saturation level for all signal strengths, which would guarantee a higher resolution at small signal strengths.

The relative shift between the signal and reference light distributions can be determined with mean wavelength estimators. Several algorithms have been evaluated. The centroid method [77] and a Gaussian correlation algorithm (which maximizes the correlation function with a Gaussian) [78] produced large systematic errors, which increased linearly with the wind speed. This phenomenon is referred to as "slope error" and is very pronounced for the FWFIMI because of the large width of the cosine-shaped fringe, which makes the shape asymmetric for small shifts. For large shifts, parts of the lineshape are not fully imaged, and the systemic errors become non-linear

(edge bias). A maximum likelihood function approach could be used as well. Least-square fits are a simple alternative that shows no slope error and no edge bias. Effects caused by the illumination function are neglected here. The experimental illumination function has to be characterized and has to be included in the final fitted model.

Here we use a "downhill simplex fit" (Nelder–Mead method [79]), which does not use derivatives and therefore converges very safely.

The fit function prior to downsampling has the form

$$f(w, x) = w_0 (1 + w_1 \cos(x + w_2)) + w_3. \tag{23}$$

Here, $w_0$, $w_1$, $w_2$, and $w_3$ are the fit parameters for amplitude, contrast, shift, and background. The quadratic sum of the data values minus the downsampled fit function $f(w, x)$ is minimized with a Nelder–Mead simplex algorithm. Wind speeds are determined by dividing $w_2(\mathrm{Ref}) - w_2(\mathrm{Sig})$ by the phase sensitivity $S$ (see Section 2.B).

A possible way to decrease the speckle contrast is the digital summation of several pulses for the signal and reference light prior to evaluation, called "mean evaluation" (ME) in the following. In contrast to the evaluation of a single pulse, "pulse evaluation" (PE), ME reduces the effective measurement rate but has the second advantage of averaging the detector noise. ME requires the thermo-mechanical stability of the setup (see Section 3) and the frequency stability of the laser during the time of digital summation. A typical Nd:YAG laser transmitter, as in WALES [38], has a pulse-to-pulse frequency jitter distribution during less than 60 s of about 1 MHz in the UV. In the case of ME, this jitter has to be considered.

The ME method is used with 0.1 s $\times$ $R_L$ pulses for one measurement [indicated by ME(0.1 s)]. Limits to the digital summation time are set by the flight speed of the aircraft ($\approx 250$ m/s). In the simulation, 50 realizations are compiled, and the mean ($\overline{u_r}$) and standard deviation $\sigma(u_r)$ of the determined wind speeds are computed. The simulated LoS wind speed is 10 m/s, which is a typical order of magnitude of wind speeds in wake vortices, or gusts within turbulence of "moderate" strength.

In the following simulations, we look at two extreme cases of a low backscattered signal ($h = 10,000$ m, $R_b = 1$) and a high backscattered signal ($h = 1000$ m, $R_b = 6$). We assume a range gate $\Delta R$ of 20 m. The calculations are done for various measurement points between 50 and 200 m, spaced by $\Delta R$. We assume a linear PMT array with 12 illuminated elements in the analog detection mode (see Section 4).

We consider a maximum current of 5 mA per pulse and element, such that the PMT elements are not damaged. In case of the WALES transmitter, the backscattered signal currents after amplification (even at low voltages) are so high that only 80% of the signal can be used in the case of $h = 10,000$ m, $R_b = 1$ and only 5% in case of $h = 1000$ m, $R_b = 6$ in order to stay below 5 mA. For a better comparability of the transmitters at $h = 10,000$ m, $R_b = 1$, we assume $\eta_T = 78\%$ for all transmitters. For "HYPO," a signal damping of 35% is necessary for high signal strengths ($h = 1000$ m, $R_b = 6$). In case of the MULTIPLY and AWIATOR transmitters, the backscattered signals do not have to be damped because of the lower pulse energies. The signal currents in this case are

kept below 5 mA by adjusting the PMT voltage between 500 and 900 V. The reference current is adjusted to below 5 mA per pulse.

Figure 11(a) shows typical SNR values of detector noise for all 12 elements of a linear PMT array (family of curves) at $h = 10,000$ m, $R_b = 1$ as a function of range $R$ for one pulse of the different laser transmitters. A respective plot is shown in Fig. 11(b) for an altitude of 1000 m and a scattering rato $R_b$ of 6.

The total atmospheric speckle patterns for the signal light ($M_{Ray} = 444$, $M_{Mie} = 20$) at $h = 10,000$ m, $R_b = 1$ and at $h = 1000$ m, $R_b = 6$ are shown in Fig. 11(c). Figure 11(d) contains exemplary downsampled speckle distributions for a single pulse and for averaging over a measurement time of 0.1 s (signal) and over 1000 pulses (reference).

Figure 12 shows the final determined range-dependent values of $\sigma(u_r)$ for these properties.

Several trends are observed considering detector noise only. The standard deviation increases as a function of range $R$ because the detector SNR decreases [see Figs. 11(a) and 11(b)]. In the case of $h = 10,000$ m, $R_b = 1$, the range dependence of the SNR is roughly proportional to $1/R$ for all the elements of the PMT array. In case of $h = 1000$ m, $R_b = 6$, the SNR dependence is close to $1/(R^{1.25})$. This trend could be explained with additional extinction from aerosols at these parameters. Seeing from Eq. (2) that the lidar signal decreases with $R^{-2}$, and knowing that the dominant shot noise scales with the square root of the signal (Gaussian behavior for large signal strengths), the $1/R$ dependence of the SNR for nearly pure molecular backscattered signals is not unexpected. $\sigma(u_r)$ is seen to increase roughly proportionally to $1/\text{SNR} = R$. Without averaging a multitude of pulses, $\sigma(u_r)$ is in the order of 2 m/s and higher, even for the high pulse energies of WALES. Therefore, only measurements with averaging for 0.1 s are plotted.

For $h = 1000$ m, $R_b = 6$, the SNR is elevated, and therefore, lower values of $\sigma(u_r)$ are achieved in the cases of MULTIPLY, AWIATOR, and HYPO. In the case of WALES,

the signal damping must be so strong that $\sigma(u_r)$ is bigger. However, a small decrease of $\sigma(u_r)$ is observed, which is probably due to the increased atmospheric contrast.

Laser jitter of 1 MHz per pulse turns out to have no significant influence on the result and can therefore be omitted.

When modeled atmospheric speckles are included, the following trends can be observed. For WALES and HYPO, $\sigma(u_r)$ is below 1 m/s up to ranges of about 120 m. HYPO performs even better mostly because the digital averaging allows more pulses during 0.1 s, while the SNR is better than for MULTIPLY and AWIATOR. HYPO seems to be closer to an optimal combination of pulse energy and repetition rate for averaging out detector and speckle noise than WALES.

At low signal strengths, the SNR per pulse of MULTIPLY and AWIATOR is very small, which increases $\sigma(u_r)$ for these two transmitters. Especially when speckle noise is considered, these low values of SNR seem to reduce the measurement performance. Averaging in the presence of speckle seems to be less effective, requiring higher signal-to-noise ratios.

At high signal strengths, MULTIPLY and AWIATOR profit from higher SNR values for each pulse and a higher number of pulses for averaging during the measurement time (0.1 s), such that WALES is outperformed.

The influence of fiber speckle is eliminated by averaging over 1000 pulses during the reference measurements, such that $\sigma(u_r)$ seems not to be elevated in comparison to the case where only atmospheric speckle are considered. No effect of the simulated crosstalk on the mean and standard deviation of the determined wind speeds is observed.

If the combined performance at $h = 10,000$ m, $R_b = 1$ and $h = 1000$ m, $R_b = 6$ is considered, "HYPO" appears to be the best choice within the considered transmitter types. Wake vortex mitigation algorithms, as proposed by Ehlers *et al.* [7], require low standard deviations of the determined wind speed in the order of 1 m/s or below. The required value of $\sigma(u_r)$ depends, however, on the choice of the activation criterion, on the scanning pattern geometry, on the spatial
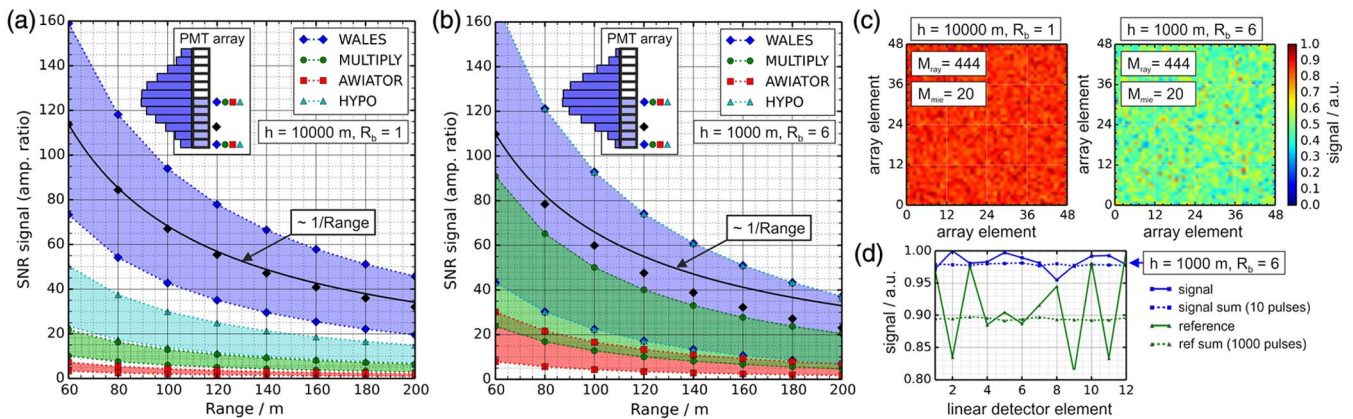


**Fig. 11.** (a) Detector SNR of one pulse for $h = 10,000$ m, $R_b = 1$ and (b) $h = 1000$ m, $R_b = 6$ in the cases of the laser transmitters: "WALES," "MULTIPLY," "AWIATOR," and "HYPO." Two curves are shown for every transmitter, giving the SNR of one center and one edge pixel of the PMT array illuminated with a centered interference fringe. Colored areas mark the regions in between where the SNR values of the other pixels are located. Additional black squares mark the SNR of the third pixel in case of WALES. The solid black line marks a range dependence of the SNR proportional to 1/Range. (c) Total speckle patterns for $h = 10,000$ m, $R_b = 1$ and for $h = 1000$ m, $R_b = 6$. (d) Exemplary downsampled speckle distribution for one WALES pulse at $h = 1000$ m, $R_b = 6$ and the respective integrated distributions on a linear detector for 10 signal pulses and 1000 reference pulses.
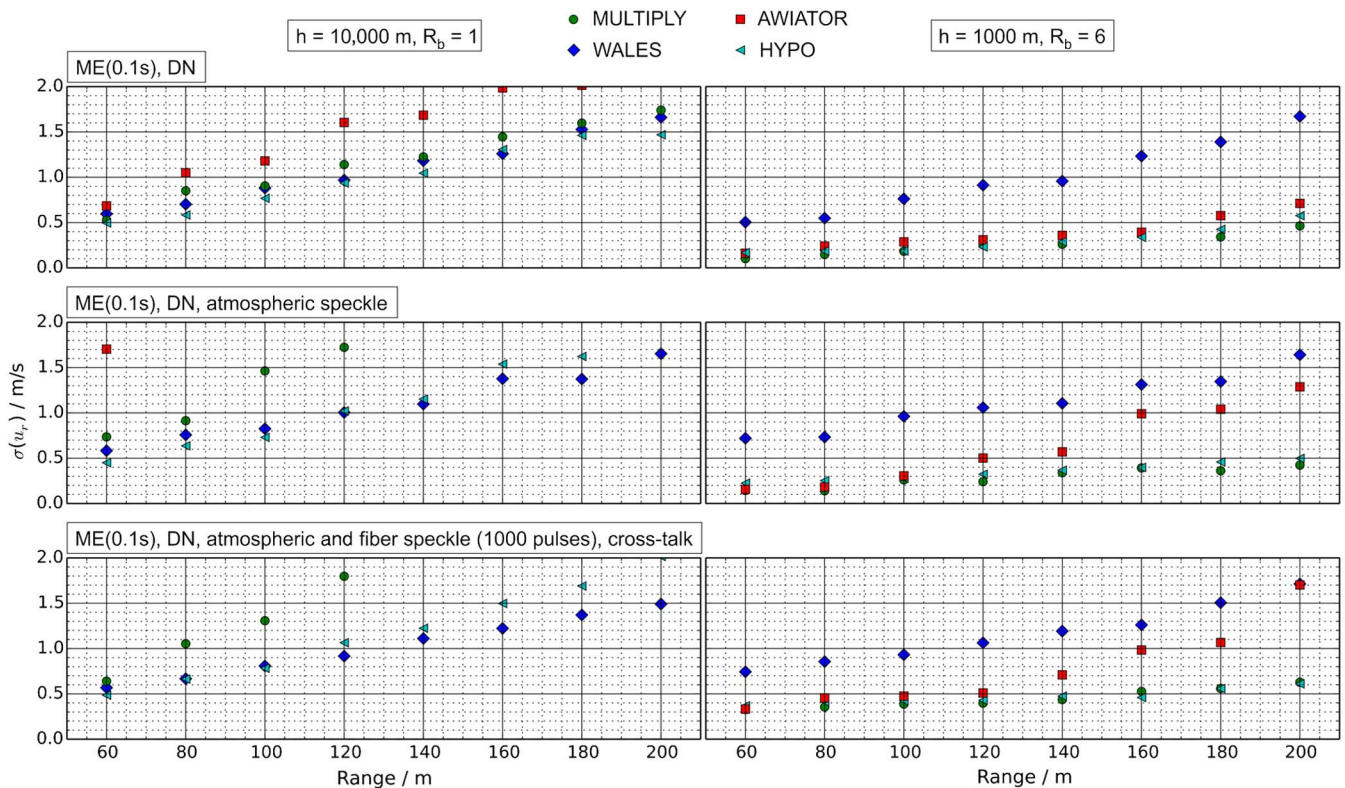
**Fig. 12.** Results of the end-to-end simulation: the standard deviation $\sigma(u_r)$ of the determined wind speed $u_r$ as a function of range $R$ for the transmitters "WALES," "MULTIPLY," "AWIATOR," and "HYPO" in case of weak backscattering signal ($h = 10,000$ m, $R_b = 1$) and strong backscattering signal ($h = 1000$ m, $R_b = 6$). $\sigma(u_r)$ is obtained by performing the simulated measurement 50 times in a row. For every measurement, digital averaging is applied for a measurement duration of 0.1 s [ME(0.1 s)]. Three cases are considered: 1. only detector noise (DN), 2. DN and atmospheric speckle, and 3. DN, atmospheric and fiber speckle, and crosstalk. In the last case, the reference measurement is averaged over 1000 pulses for every transmitter type.

resolution, and on the update rate [8,10]. Considering an averaging time of 0.1 s for one LoS measurement and a range gate length of 20 m, up to four range-resolved, exploitable measurement points can be obtained for wake vortex mitigation per LoS direction independent of the atmospheric conditions. The laser transmitter should be optimized for shorter averaging times, such that lower standard deviations and full scan update rates of 5–10 Hz can be achieved. Measurement points at greater distances ($R > 140$ m) could be also considered with lower weights and could be compared to or fusioned with the results of the next measurement cycles when the aircraft has moved closer. Gust alleviation algorithms have more relaxed requirements on the standard deviation, such that the exploitable range would be higher [9,10].

Different algorithms should be tested and an experimentally determined illumination function should be included in the final mean wavelength estimator algorithm. Future investigations should also include a performance evaluation of the FWFIMI in a tilted configuration with a second detector. We expect a reduced number of pulses to be necessary for averaging.

## 6. CONCLUSION

We have reviewed different direct DWL techniques and consider a fringe-imaging Michelson interferometer with inclined mirrors (FIMI) a good compromise between theoretical performance

and complexity, for range-resolved measurements of LoS wind speeds in the near-field (50–300 m) in front of an aircraft.

We pointed out the need for field widening in case of near-field detection and thus a large required FOV. We estimated the non-negligible bias (>0.4 m/s per μrad) of the measured wind speed induced by a laser-telescope misalignment. We have described the design principles of a tilted FIMI with field widening and temperature compensation and discussed fabrication specifications and tolerances, the illumination function, fringe localization, and their influence on the instrumental contrast. A net inclination angle between the mirrors of the FWFIMI provides linear fringes, which can be imaged on fast, linear detectors for range-resolved detection independent of the flight altitude and scattering ratio. We have proposed a scheme for incorporating the FWFIMI in free-beam and fiber-coupled receiver setups. A scrambling fiber could allow imaging independent of range and laser telescope misalignments.

The performance of the setup using only one output has been estimated, taking into account losses, detector noise, and cross talk, a simplified model for atmospheric speckle and fiber speckle, different transmitter types, and different atmospheric conditions (altitudes, scattering ratios). Temperature compensation will allow for averaging over several pulses, which is necessary to reduce the standard deviations caused by detector noise and speckle "noise." The transmitters "WALES" and

"HYPO" prospect range-resolved LoS Doppler wind measurements with standard deviations of the determined wind speed in the order of 1 ms$^{-1}$ or below independent of the atmospheric conditions at distances between 60 and 120 m, considering a range gate of 20 m and a simulated wind speed of 10 m/s and an averaging time of 0.1 s. This is important because low standard deviations are considered necessary for wake vortex alleviation control [8]. It should be evaluated if standard deviations above 1 ms$^{-1}$ at distances between 120 and 300 m can be useful for alleviation control. In order to reach the required full scan update rate of 5–10 Hz [8], an optimization of the lidar transmitter, of possible scanning patterns (at least three line-of-sight measurements required), and of the proposed receiver should be evaluated. A second detector at output 2 of the tilted FWFIMI is expected to enhance the overall measurement performance.

Future works are aimed at realizing a receiver prototype, including an FWFIMI for range-resolved LoS wind speed measurements.

## REFERENCES

1. Airbus Customer Services, "Flight operations briefing notes—adverse weather operations—optimum use of the weather radar," http://www.airbus.com/fileadmin/media_gallery/files/safety_library_items/AirbusSafetyLib_-FLT_OPS-ADV_WX-SEQ07.pdf (2007).
2. J. Baynes and P. Tyrdy, "Rockwell Collins multiscan threattrack TM weather radar," Rockwell Collins Press release (4 February 2014. https://www.rockwellcollins.com/Data/News/2014_Cal_Year/CS/FY14CSNR22-ThreatTrack.aspx.
3. A. P. Tvaryanas, "Epidemiology of turbulence-related injuries in airline cabin crew," Aviat. Space Environ. Med. **74**, 970–976 (2003).
4. J. K. Evans, "An updated examination of aviation accidents associated with turbulence, wind shear and thunderstorm," AMA-RPT No. 14-14, NF1676L-20566 (Analytical Mechanics Associates, Inc., 2014) http://ntrs.nasa.gov/search.jsp?R=20160005906.
5. F. Holzäpfel, A. Stephan, T. Heel, and S. Körner, "Enhanced wake vortex decay in ground proximity triggered by plate lines," Aircr. Eng. **88**, 206–214 (2016).
6. G. Looye, T. Lombaerts, and T. Kier, "Design and flight testing of feedback control laws," Research Report 2012-02 (The DLR Project Wetter & Fliegen, German Aerospace Center, 2012), pp. 162–170.
7. J. Ehlers, D. Fischenberg, and D. Niedermeier, "Wake impact alleviation control based on wake identification," J. Aircr. **52**, 2077–2089 (2015).
8. J. Ehlers and N. Fezans, "Airborne Doppler lidar sensor parameter analysis for wake vortex impact alleviation purposes," in *Advances in Aerospace Guidance, Navigation and Control: Selected Papers of the Third CEAS Specialist Conference on Guidance, Navigation and Control held in Toulouse*, J. Bordeneuve-Guibé, A. Drouin, and C. Roos, eds. (Springer, 2015), pp. 433–453.
9. J. Schwithal and N. Fezans, Institut für Flugsystemtechnik (FT), German Aerospace Center (DLR), Lilienthalplatz 7, 38108 Braunschweig, Germany (personal communication, 2016).
10. N. Fezans, J. Schwithal, and D. Fischenberg, "In-flight remote sensing and characterization of gusts, turbulence, and wake vortices," in *Deutscher Luft- und Raumfahrtkongress*, Rostock, Germany, 2015.
11. S. I. N. Banakh and A. Viktor, *Coherent Doppler Wind Lidars in a Turbulent Atmosphere* (Artech House, 2013).
12. V. A. Banakh, I. N. Smalikho, and C. Werner, "Effect of aerosol particle microstructure on cw Doppler lidar signal statistics," Appl. Opt. **39**, 5393–5402 (2000).
13. R. L. McCally, "Laser eye safety research at apl," Johns Hopkins APL Tech. Dig. **26**, 46–55 (2005).
14. O. Reitebuch, C. Werner, I. Leike, P. Delville, P. H. Flamant, A. Cress, and D. Engelbart, "Experimental validation of wind profiling performed by the airborne 10-μm heterodyne Doppler lidar wind," J. Atmos. Ocean. Technol. **18**, 1331–1344 (2001).
15. F. Köpp, S. Rahm, and I. Smalikho, "Characterization of aircraft wake vortices by 2-μm pulsed Doppler lidar," J. Atmos. Ocean. Technol. **21**, 194–206 (2004).
16. H. Inokuchi, H. Tanaka, and T. Ando, "Development of an onboard Doppler lidar for flight safety," J. Aircr. **46**, 1411–1415 (2009).
17. H. Inokuchi, M. Furuta, and T. Inagaki, "High altitude turbulence detection using an airborne Doppler lidar," in *29th Congress of the International Council of the Aeronautical Sciences (ICAS)*, St. Petersburg, Russia, 7–12 September 2014.
18. I. N. Smalikho, V. A. Banakh, F. Holzäpfel, and S. Rahm, "Method of radial velocities for the estimation of aircraft wake vortex parameters from data measured by coherent Doppler lidar," Opt. Express **23**, A1194–A1207 (2015).
19. A. Behrendt, S. Pal, V. Wulfmeyer, A. Valdebenito, and G. Lammel, "A novel approach for the characterization of transport and optical properties of aerosol particles near sources– i. measurement of particle backscatter coefficient maps with a scanning UV lidar," Atmos. Environ. **45**, 2795–2802 (2011).
20. C. Flesia and C. L. Korb, "Theory of the double-edge molecular technique for Doppler lidar wind measurement," Appl. Opt. **38**, 432–440 (1999).
21. Y. Durand, R. Meynart, M. Endemann, E. Chinal, D. Morançais, T. Schröder, and O. Reitebuch, "Manufacturing of an airborne demonstrator of ALADIN: the direct detection Doppler wind lidar for ADM-aeolus," Proc. SPIE **5984**, 598401 (2005).
22. N. P. Schmitt, W. Rehm, T. Pistner, P. Zeller, H. Diehl, and P. Nav'e, "The awiator airborne lidar turbulence sensor," Aerosp. Sci. Technol. **11**, 546–552 (2007).
23. G. J. Rabadan, N. P. Schmitt, T. Pistner, and W. Rehm, "Airborne lidar for automatic feedforward control of turbulent in-flight phenomena," J. Aircr. **47**, 392–403 (2010).
24. M. C. Hirschberger and G. Ehret, "Simulation and high-precision wavelength determination of noisy 2D Fabry-Perot interferometric rings for direct-detection Doppler lidar and laser spectroscopy," Appl. Phys. B **103**, 207–222 (2011).
25. J. A. McKay, "Assessment of a multibeam fizeau wedge interferometer for Doppler wind lidar," Appl. Opt. **41**, 1760–1767 (2002).
26. Z. Liu and T. Kobayashi, "Differential discrimination technique for incoherent Doppler lidar to measure atmospheric wind and backscatter ratio," Opt. Rev. **3**, 47–52 (1996).
27. D. Bruneau, "Mach-Zehnder interferometer as a spectral analyzer for molecular Doppler wind lidar," Appl. Opt. **40**, 391–399 (2001).
28. D. Bruneau, "Fringe-imaging Mach-Zehnder interferometer as a spectral analyzer for molecular Doppler wind lidar," Appl. Opt. **41**, 503–510 (2002).
29. D. Bruneau and J. Pelon, "Simultaneous measurements of particle backscattering and extinction coefficients and wind velocity by lidar with a Mach-Zehnder interferometer: principle of operation and performance assessment," Appl. Opt. **42**, 1101–1114 (2003).
30. C. J. Grund and S. Tucker, "Optical autocovariance wind lidar (OAWL): a new approach to direct-detection Doppler wind profiling," in *Fifth Symposium on Lidar Atmospheric Applications*, Seattle, Washington (American Meteorological Society, 2011).

31. R. Atlas, R. N. Hoffman, Z. Ma, G. D. Emmitt, and S. A. Wood, Jr., S. Greco, S. Tucker, L. Bucci, B. Annane, R. M. Hardesty, and S. Murillo, "Observing system simulation experiments (osses) to evaluate the potential impact of an optical autocovariance wind lidar (OAWL) on numerical weather prediction," J. Atmos. Ocean. Technol. **32**, 1593–1613 (2015).

32. J. A. Smith and X. Chu, "Investigation of a field-widened Mach-Zehnder receiver to extend Fe Doppler lidar wind measurements from the thermosphere to the ground," Appl. Opt. **55**, 1366–1380 (2016).

33. N. Cézard, A. Dolfi-Bouteyre, J.-P. Huignard, and P. H. Flamant, "Performance evaluation of a dual fringe-imaging Michelson interferometer for air parameter measurements with a 355 nm Rayleigh–Mie lidar," Appl. Opt. **48**, 2321–2332 (2009).

34. G. Hansen, "Die sichtbarkeit der interferenzen beim Michelson- und Twyman-interferometer," Zeitschrift für Instrumentenkunde **61**, 411 (1941).

35. R. L. Hilliard and G. G. Shepherd, "Wide-angle Michelson interferometer for measuring Doppler line widths*," J. Opt. Soc. Am. **56**, 362–369 (1966).

36. G. G. Shepherd, W. A. Gault, D. W. Miller, Z. Pasturczyk, S. F. Johnston, P. R. Kosteniuk, J. W. Haslett, D. J. W. Kendall, and J. R. Wimperis, "Wamdii: wide-angle Michelson Doppler imaging interferometer for spacelab," Appl. Opt. **24**, 1571–1584 (1985).

37. J. M. Harlander, C. R. Englert, D. D. Babcock, and F. L. Roesler, "Design and laboratory tests of a Doppler asymmetric spatial heterodyne (DASH) interferometer for upper atmospheric wind and temperature observations," Opt. Express **18**, 26430–26440 (2010).

38. M. Wirth, A. Fix, P. Mahnke, H. Schwarzer, F. Schrandt, and G. Ehret, "The airborne multi-wavelength water vapor differential absorption lidar wales: system design and performance," Appl. Phys. B **96**, 201–213 (2009).

39. P. Vrancken, M. Wirth, B. Ehret, G. Witschas, H. Veermann, R. Tump, H. Barny, P. Rondeau, A. Dolfi-Bouteyre, and L. Lombard, "Flight tests of the delicate airborne lidar system for remote clear air turbulence detection," in *27th International Laser Radar Conference*, New York, 2015.

40. D. Bruneau, J. Pelon, F. Blouzon, J. Spatazza, P. Genau, G. Buchholtz, N. Amarouche, A. Abchiche, and O. Aouji, "355-nm high spectral resolution airborne lidar LNG: system description and first results," Appl. Opt. **54**, 8776 (2015).

41. G. Avila and P. Singh, "Optical fiber scrambling and light pipes for high accuracy radial velocities measurements," Proc. SPIE **7018**, 70184W (2008).

42. B. Witschas, "Light scattering on molecules in the atmosphere," in *Atmospheric Physics: Background–Methods–Trends*, U. Schumann, ed. (Springer, 2012), pp. 69–83.

43. T. Wriedt, "Mie theory: a review," in *The Mie Theory: Basics and Applications*, W. Hergert and T. Wriedt, eds. (Springer, 2012), pp. 53–71.

44. R. B. Miles, W. R. Lempert, and J. N. Forkey, "Laser Rayleigh scattering," Meas. Sci. Technol. **12**, R33 (2001).

45. M. H. Rausch, A. Heller, J. Herbst, T. M. Koller, M. Bahlmann, P. S. Schulz, P. Wasserscheid, and A. P. Fröba, "Mutual and thermal diffusivity of binary mixtures of the ionic liquids [BMIM][C(CN)$_3$] and [BMIM][B(CN)$_4$] with dissolved $CO_2$ by dynamic light scattering," J. Phys. Chem. B **118**, 4636–4646 (2014).

46. S. Groß, V. Freudenthaler, M. Wirth, and B. Weinzierl, "Towards an aerosol classification scheme for future earthcare lidar observations and implications for research needs," Atmos. Sci. Lett. **16**, 77–82 (2015).

47. G. Tenti, C. D. Boley, and R. C. Desai, "On the kinetic model description of Rayleigh-Brillouin scattering from molecular gases," Can. J. Phys. **52**, 285–290 (1974).

48. B. Witschas, "Analytical model for Rayleigh-Brillouin line shapes in air," Appl. Opt. **50**, 267–270 (2011).

49. R. T. H. Collis and P. B. Russell, "Lidar measurement of particles and gases by elastic backscattering and differential absorption," in *Laser Monitoring of the Atmosphere*, E. D. Hinkley, ed., Vol. **14** of Topics in Applied Physics, (Springer, 1976), pp. 71–151.

50. A. Bucholtz, "Rayleigh-scattering calculations for the terrestrial atmosphere," Appl. Opt. **34**, 2765–2773 (1995).

51. J. M. Vaughan, D. W. Brown, C. Nash, S. B. Alejandro, and G. G. Koenig, "Atlantic atmospheric aerosol studies: 2. compendium of airborne backscatter measurements at 10.6 μm," J. Geophys. Res. **100**, 1043–1065 (1995).

52. D. J. Moorhouse and R. J. Woodcock, "Background information and user guide for MIL-F-8785C, military specification-flying qualities of piloted airplanes," No. AFWAL-TR-81-3109 (Air Force Wright Aeronautical Labs Wright-Patterson Air Force Base, 1982)..

53. R. M. Measures, *Laser Remote Sensing* (Wiley, 1992).

54. M. I. Mishchenko, "Directional radiometry and radiative transfer: The convoluted path from centuries-old phenomenology to physical optics," J. Quant. Spectrosc. Radiat. Transfer **146**, 4–33 (2014).

55. U. Paffrath, C. Lemmerz, O. Reitebuch, B. Witschas, I. Nikolaus, and V. Freudenthaler, "The airborne demonstrator for the direct-detection Doppler wind lidar ALADIN on ADM-aeolus. part ii: Simulations and Rayleigh receiver radiometric performance," J. Atmos. Ocean. Technol. **26**, 2516–2530 (2009).

56. J. A. McKay, "Modeling of direct detection Doppler wind lidar. i. the edge technique," Appl. Opt. **37**, 6480–6486 (1998).

57. M. J. McGill and J. D. Spinhirne, "Comparison of two direct-detection Doppler lidar techniques," Opt. Eng. **37**, 2675–2686 (1998).

58. J. A. McKay, "Modeling of direct detection Doppler wind lidar. ii. the fringe imaging technique," Appl. Opt. **37**, 6487–6493 (1998).

59. J. Wu, J. Wang, and P. B. Hays, "Performance of a circle-to-line optical system for a Fabry-Perot interferometer: a laboratory study," Appl. Opt. **33**, 7823–7828 (1994).

60. O. Reitebuch, C. Lemmerz, E. Nagel, U. Paffrath, Y. Durand, M. Endemann, F. Fabre, and M. Chaloupy, "The airborne demonstrator for the direct-detection Doppler wind lidar ALADIN on ADM-aeolus. Part I: instrument design and comparison to satellite instrument," J. Atmos. Ocean. Technol. **26**, 2501–2515 (2009).

61. O. Reitebuch, Institut für Physik der Atmosphäre (IPA), German Aerospace Center (DLR), Oberpfaffenhofen, Münchner Str. 20, 82234 Wessling, Germany (personal communication, 2016).

62. K. Stelmaszczyk, M. Dell'Aglio, S. Chudzyński, T. Stacewicz, and L. Wöste, "Analytical function for lidar geometrical compression form-factor calculations," Appl. Opt. **44**, 1323–1331 (2005).

63. O. Novák, I. S. Falconer, R. Sanginés, M. Lattemann, R. N. Tarrant, D. R. McKenzie, and M. M. M. Bilek, "Fizeau interferometer system for fast high resolution studies of spectral line shapes," Rev. Sci. Instrum. **82**, 023105 (2011).

64. A. M. Title, "Imaging Michelson interferometers," in *Observing Photons in Space: A Guide to Experimental Space Astronomy*, M. C. E. Huber, A. Pauluhn, J. L. Culhane, J. G. Timothy, K. Wilhelm, and A. Zehnder, eds. (Springer, 2013), pp. 349–361.

65. A. M. Title and H. E. Ramsey, "Improvements in birefringent filters. 6: analog birefringent elements," Appl. Opt. **19**, 2046–2058 (1980).

66. Z. Cheng, D. Liu, J. Luo, Y. Yang, Y. Zhou, Y. Zhang, L. Duan, L. Su, L. Yang, Y. Shen, K. Wang, and J. Bai, "Field-widened Michelson interferometer for spectral discrimination in high-spectral-resolution lidar: theoretical framework," Opt. Express **23**, 12117–12134 (2015).

67. SCHOTT, "Refractive index and dispersion," SCHOTT Technical Information, TIE-29, 2007.

68. SCHOTT, "Temperature coefficient of the refractive index," SCHOTT Technical Information, TIE-19, 2008.

69. S. Mahadevan, J. Ge, C. DeWitt, J. C. van Eyken, and G. Friedman, "Design of a stable fixed delay interferometer prototype for the ET project," Proc. SPIE **5492**, 615–623 (2004).

70. X. Wan, J. Ge, and Z. Chen, "Development of stable monolithic wide-field Michelson interferometers," Appl. Opt. **50**, 4105–4114 (2011).

71. J. M. Harlander and C. Englert, "Design of a real-fringe DASH interferometer for observations of thermospheric winds from a small satellite," in *Imaging and Applied Optics*, OSA Technical Digest (online) (Optical Society of America, 2013), paper FW1D.2.

72. D. Liu, C. Hostetler, I. Miller, A. Cook, and J. Hair, "System analyis of a tilted field-widened Michelson interferometer for high spectral resolution lidar," Opt. Express **20**, 1406–1420 (2012).

73. G. Fortunato, "L'interféromètre de Michelson, quelques aspects théoriques et expérimentaux," Bulletin de l'Union des Physiciens **91**, 15–56 (1997).

74. J. W. Goodman, *Speckle Phenomena in Optics: Theory and Applications* (Roberts & Company, 2007).

75. L. Rodriguez-Cobo, M. Lomer, C. Galindez, and J. M. Lopez-Higuera, "Speckle characterization in multimode fibers for sensing applications," Proc. SPIE **8413**, 84131R (2012).

76. Hamamatsu, *PMT Handbook*, version 3 (Hamamatsu Photonics, 2007).

77. J.-M. Gagné, J.-P. Saint-Dizier, and M. Picard, "Méthode d'echantillonnage des fonctions déterministes en spectroscopie: application à un spectromètre multicanal par comptage photonique," Appl. Opt. **13**, 581–588 (1974).

78. U. Paffrath, "Performance assessment of the Aeolus Doppler wind lidar prototype," Dissertation DLR-FB–2006-2012 (DLR-Forschungsbericht, 2006).

79. J. A. Nelder and R. Mead, "A simplex method for function minimization," Comput. J. **7**, 308–313 (1965).